ELSEVIER

Available online at www.sciencedirect.com

SCIENCE DIRECT

Journal of Sound and Vibration 283 (2005) 589–620

JOURNAL OF SOUND AND VIBRATION

www.elsevier.com/locate/jsvi

Galerkin-based modal analysis on the vibration of wire–slurry system in wafer slicing using a wiresaw

Liqun Zhu, Imin Kao*

Department of Mechanical Engineering, State University of New York at Stony Brook, Stony Brook, NY 11794-2300, USA

Received 4 June 2003; accepted 30 April 2004

Abstract

Wiresaws have been widely used in industries to slice semiconductor ingots into thin wafers for semiconductor fabrication. However, the surface roughness of a wiresaw-sliced wafer is usually not uniform which can be a concern in the subsequent lapping and polishing processes. It is sometimes observed that poor surface finish can occur at the beginning and the end of sliced round wafers when contact spans are short. In this paper, the dynamics of a coupled wire/slurry non-conservative vibration system is analyzed according to the rolling-indenting floating machining mechanism of typical wiresaw processes. Basic approaches adopted are the linearization of the coupled nonlinear governing equations with respect to the equilibrium, Galerkin-based discretization of the distributed non-conservative system, and the subsequent modal analysis. For the purpose of model verification, a numerical scheme of direct-time integration to an alternative finite element (FE) semi-discretized system is performed using the one-step Newmark's method. The results from the eigenanalysis of the Galerkin-based model are presented. These simulation results indicate that the wire/slurry system consists of both real and paired complex eigenvalues, which correspond to the over-damped modes and other vibration modes of the system. Parametric studies show that the vibration displacement of the wire decreases when the contact span expands, which explains the typical distribution of the surface roughness of a round wiresawn wafer. From the parametric studies, the tension and bow angle of the wire are found to play important roles in the response of the wire. Finally, in order to reduce the differential saw damage caused by the vibration of the wire, adaptive vibration control strategies are proposed for the wiresaw slicing processes.

© 2004 Elsevier Ltd. All rights reserved.

*Corresponding author. Tel.: +1-631-632-8308; fax: +1-631-632-8544.
E-mail address: kao@mal.eng.sunysb.edu (I. Kao).

0022-460X/$ - see front matter © 2004 Elsevier Ltd. All rights reserved.
doi:10.1016/j.jsv.2004.04.018

Nomenclature

C_1, C_2	constants depending on the geometry of the cross-section of the wire
EU	error function in the vibration displacement field of wire
EP	error function in the transient pressure field of slurry
f	external excitation acting on the wire
f_p	distributed force generated from the slurry pressure
f_{tot}	total distributed force acting on the wire
f_0	amplitude of the external excitation f
g	geometric mapping factor
h	total thickness of the slurry film
h_0	equilibrium thickness of the slurry film
L	length of wire between wire guides
L'	contact span, between wire and ingot surface at contact interface
m	mass density of wire per unit length
MRR	material removal rate
NF	number of the concentrated forces after discretizing the distributed external excitation f
N_n	nominal cutting force generated from the bow angle and tension of the wire
NP	number of terms in the Fourier expansion of the transient slurry pressure
NU	number of terms in the Fourier expansion of the wire vibration displacement
p	transient hydrodynamic pressure in the slurry film
P	total hydrodynamic pressure in the slurry film
P_{avg}	average slurry pressure at equilibrium
P_0	equilibrium hydrodynamic pressure in the slurry film
q_0	amplitude of the concentrated forces after discretizing the distributed external excitation f
R_a	average surface roughness
r_j	jth Fourier coefficient in the Fourier expansion of the transient slurry pressure
T	wire tension
U	transverse displacement of wire
u_j	jth Fourier coefficient in the Fourier expansion of wire vibration displacement U
U_{tot}	total transverse displacement of wire
U_0	equilibrium displacement of wire
V	speed of wire
α	bow angle of wire
β	the ratio between the magnitude of the external excitation and the nominal cutting load
ω_f	frequency of the external excitation f
μ	dynamic viscosity of the slurry flow
ϕ	shape (basis) function used in the Fourier expansion of wire vibration displacement
ψ	shape (basis) function in the Fourier expansion of the transient slurry pressure

1. Introduction

Wiresaw slicing technology has been playing an important role in crystal wafer production since the early 1990s. Being capable of slicing large (in diameter) and very thin (in thickness) wafers made of various materials, wiresaws have been employed widely in photovoltaic and semiconductor manufacturing. In addition, wiresaws have also been applied in slicing sapphire, III–V compound, silicon carbide, lithium niobate, and other wafers. According to the rolling-indenting model [1–5] for material removal, slicing using a wiresaw has many unique advantages over other wafer-slicing processes (such as slicing with the inner diameter or ID saws). These advantages include high throughput batch slicing, less wafer surface damage, and lower kerf loss.

A schematic of the modern wiresaw process is shown in Fig. 1. During the wiresaw slicing process, a wire web comprised of a few hundreds of parallel strands of wire is fed through the crystal ingot, which creates a small bow on the wire web. The wire web is formed by winding a single wire over four (or three) wire guides on cylindrical capstans, as shown in Fig. 1. The wire moves back-and-forth with a top speed of 10–15 m/s at steady state, while maintaining a high and constant wire tension at 20–35 N. In the mean time, abrasive-carrying slurry is supplied to the slicing zone by the slurry manifold and through the motion of the wire. As a result, a typical three-body abrasion environment is formed at the slicing interface consisting of wire, hydrodynamic slurry film, and the wire recess on the crystal ingot.

In this paper, we present the analysis of vibration of the wire in the slurry wiresaw process when the wire is subjected to an external excitation, which can result from the multi-point contacts between the wire and abrasive particles/impurities in the slurry or from other system noises. Compared to our previous studies [6,7], we present new results of coupled hydrodynamic and vibration analysis by taking into consideration the effects of the abrasive carrying slurry on the vibration characteristics of the wire. These effects include non-classical (in the sense that the modes are complex) damping and an added stiffness. Basic theoretical model is constructed by coupling the vibration equation of the wire and the nonlinear Reynold's equation describing the tribological behavior of the slurry flow.

Linear and nonlinear vibration behaviors of a translating media (string, sheet, beam, etc.) have been studied since the early 1990s. The vibration of a moving media which is directly related to the wiresaw process has been studied in Refs. [3,7–12]. The vibration response of a moving wire subjected to simple viscous damping and harmonic excitations was studied in Ref. [7]. The extensive studies of foil bearing systems have provided valuable knowledge regarding the dynamics of an elasto-hydrodynamic lubricated moving media. For example, the free linear vibration analysis has been conducted in Ref. [9] to investigate the dynamics of the head/tape coupled system. The author's approach has provided efficient means of evaluating the natural frequencies, damping, and mode shape of the tape displacement and the pressure of the air bearing. Basic approaches adopted in Ref. [9] include the system linearization, the global Galerkin-based discretization, and the general eigenvalue analysis. Furthermore, the effects of tape translating speed and the position of the head on the system dynamics were analyzed. Recently, Galerkin-based modal analysis was

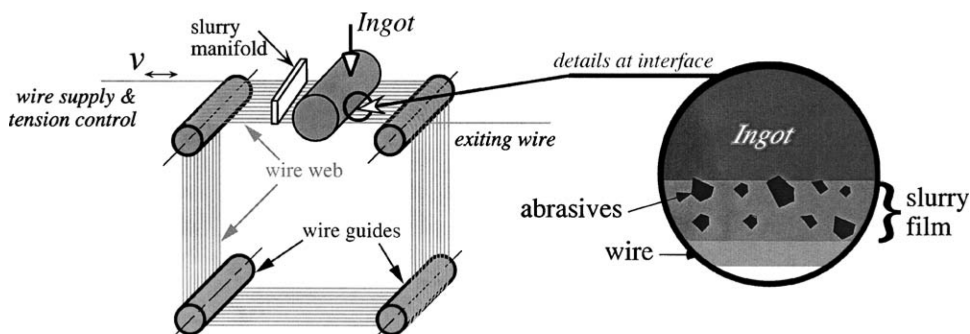

Fig. 1. Schematic of the modern wiresaw system and the details at the contact interface.

proven to be a useful tool in the vibration analysis of linear and nonlinear distributed-parameter systems [13–15]. Compared to other alternatives such as direct-time integration, the Galerkin-based modal analysis is more systematic and physically intuitive with reduced computation cost.

This paper discusses the forced vibration of a wire in a slurry wiresaw process by taking into account the elasto-hydrodynamic interaction at the wire/slurry interface. Similar to Ref. [9], basic approaches adopted in this paper include Galerkin-based discretization and the subsequent modal analysis of the non-conservative system obtained through the linearization about equilibrium. The Galerkin-discretized model is verified by applying an alternative direct-time integration scheme using Newmark's method to piecewise-interpolated the finite element (FE) semi-discretized system. Combining our elasto-hydrodynamic analysis of the equilibrium wire/slurry system [6,16] and this Galerkin-based model, the vibration characteristics of the wire is studied when it is subject to distributed harmonic excitations acting along the contact span. The simulation results indicate that the tendency of higher surface roughness occurs when the contact spans are small near the wire's initial engaging and exiting parts of the wafers with circular cross-section. This is confirmed by the statistical measurement of the surface roughness of a typical wiresaw-sliced silicon wafer. Next, important process parameters affecting the vibration of the wire are identified and investigated through parametric studies. In order to avoid excessive vibration of the wire and to obtain uniform low roughness over wiresaw sliced wafers, adaptive control strategies for adjusting process parameters during the wiresaw slicing processes are proposed in Section 5.

2. Theoretical modeling

2.1. Computational model

In the wafer slicing process using slurry wiresaws, the wire is usually made of plain carbon steel with a typical diameter of 150–175 μm and low mass density per unit length (typically 0.1876 g/m). The computational model of a typical wiresaw slicing process is shown in Fig. 2. During steady slicing, the wire is subject to high tension T (20–35 N) and moves with a constant speed V (10–15 m/s) between two rotating wire guides. During the slicing process, the wire reverses directions periodically in order to slice through the crystal ingot, which can take 4–6 h typically. However, over 90% of time the wire moves in one direction at top speed. Our modeling is focused on this period of cutting operation when the wire travels at the constant top speed along one direction. The slicing performed during the transition, the brief period for reversing directions, is minimal and will be neglected in the analysis.

The computational model of wire on ingot is shown in Fig. 2, in which the fixed distance separating the two wire guides is L. The axial translation ($+X$ direction in Fig. 2) of the wire together with the vertical cutting force generated by the bow angle α and tension of wire T cause a thin slurry film to be trapped in the narrow gap between the wire and the wire recess on the surface of the ingot substrate. The bow angle of wire is kept small (about 2°–4°) during slicing processes. With such a small bow, the tool mark (or cut profile of the wire) along the axial direction is nearly a circular arc of very large radius of

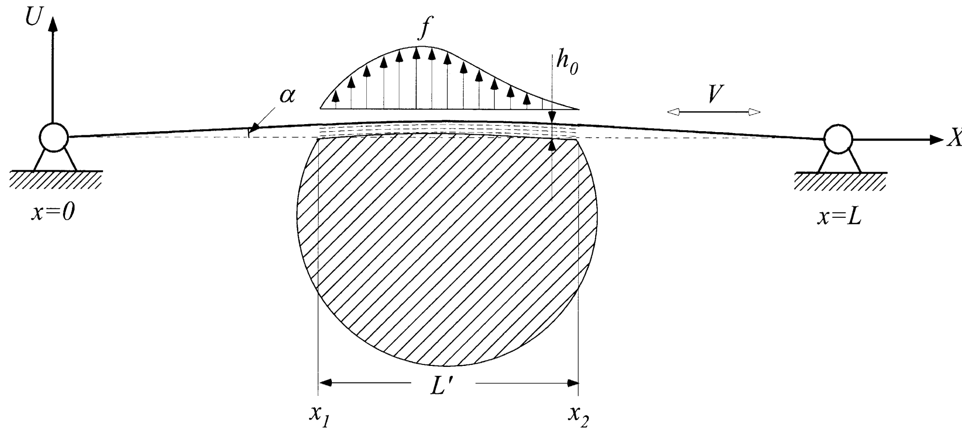

Fig. 2. Computational model for the vibration analysis of the wire in wiresaw process.

curvature (typically larger than 2 m for 100 mm contact span). Therefore, the tool marks on the ingot substrate can be safely assumed as flat ($\mathrm{d}\delta(x)/\mathrm{d}x \approx 0$, where $\delta(x)$ is the tool mark on the ingot) with its length being the contact span L' (from x_1 to x_2). Without loss of generality, the vertical feeding of ingot ($+U$ direction) is considered as quasi-static, i.e., the ingot substrate stays stationary and is separated from the moving wire by a distance h_0. Note under floating machining condition (the wire is fully supported by the hydrodynamic pressure of the slurry flow) of normal slicing, this h_0 is the thickness of developed slurry film between the wire and ingot recess. Usually it is a function of x [6,16]. During wiresaw slicing, the wire undergoes transverse vibration (U direction) due to the distributed external excitation f along the contact span. The excitation may come from the contacts of abrasive particles (featured by "direct-contact" and "semi-direct contact" when the cutting load is supported entirely or partially by the abrasive particles instead of the hydrodynamic pressure of the slurry film) and/or other system noises.

2.2. Theoretical formulation

As presented in Refs. [7,11], the transverse motion of an axially moving string can be described by the following partial differential equation:

$$
\begin{aligned}
m \frac{\partial^2 U_{\mathrm{tot}}(x,t)}{\partial t^2} + 2mV \frac{\partial^2 U_{\mathrm{tot}}(x,t)}{\partial x \partial t} - (T - mV^2) \frac{\partial^2 U_{\mathrm{tot}}(x,t)}{\partial x^2} \\
= f_{\mathrm{tot}}(x,t)[H_{x1}(x) - H_{x2}(x)], \quad (0 \leqslant x \leqslant L),
\end{aligned} \tag{1}
$$

where U_{tot} is the transverse displacement of the wire, m is the mass density of the wire per unit length, V is the speed of the wire along the $+X$ direction, T is the tension of the wire, f_{tot} is the distributed force acting transversely on the wire, and H stands for *Heaviside* function. Due to the high tension and low mass density of the wire, the translating speed, V, of the wire is

low enough so that it plays very limited role in the transverse vibration characteristics.[1] Therefore, the connective acceleration term in Eq. (1) can be safely removed in order to reduce the complexity of the analysis. This leads to the dynamic equation describing the transverse vibration of a stationary wire

$$m\frac{\partial^2 U_{\text{tot}}(x,t)}{\partial t^2} - T\frac{\partial^2 U_{\text{tot}}(x,t)}{\partial x^2} = f_{\text{tot}}(x,t)[H_{x1}(x) - H_{x2}(x)], \quad (0 \leqslant x \leqslant L). \tag{2}$$

The flexural rigidity of the wire is neglected in both Eqs. (1) and (2) due to the very small cross-section area of the wire. According to the nature of the wiresaw processes, the distributed force acting transversely on the wire is composed of two parts [6,16,17]:

$$f_{\text{tot}}(x,t) = f(t) + f_p(x,t), \tag{3}$$

where $f_p(x,t)$ is the distributed force generated from the hydrodynamic pressure in the slurry film and $f(t)$ is the external excitation resulting from the multiple contacts between the wire and the abrasive particles and/or other system noises. Without loss of generality, $f(t)$ is assumed to be harmonic with an amplitude f_0 and a frequency ω_f. It can be expressed as

$$f(t) = f_0 e^{i\omega_f t}. \tag{4}$$

Essentially, the slurry flow trapped between the wire and its recess on the ingot substrate is a 2D flow. From the finite-element analysis of the equilibrium elasto-hydrodynamic interaction in the wiresaw process [6,16], however, the slurry pressure is nearly constant along the lower circumference of the wire cross-sections except at the boundaries of the slurry film where the pressure suddenly tapers to zero (see also Section 2.3). This kind of pressure profile indicates that the hydrodynamic properties of the slurry flow are close to that of 1D incompressible laminar flow. To simplify the model, therefore, we can flatten the lower half of the cross-section of the wire (which is in contact with the slurry film) into a 2D computational domain. It forms a shape similar to a limited-width foil bearing as shown in Fig. 3. The hydrodynamic pressure inside the slurry film is assumed to be distributed uniformly along the width (Y direction) of this 2D domain [18]. Next, this hydrodynamic pressure is mapped back to the semi-circular contact area of the wire and the slurry film according to the corresponding geometry. Therefore, the distributed force resulting from the slurry pressure can be obtained by integrating the mapped hydrodynamic pressure as

$$f_p(x,t) = 2\int_0^{b/2} P(x,t)g(y)\,dy, \tag{5}$$

where $P(x,t)$ is the hydrodynamic pressure in the slurry film, b is the half circumference of the wire cross-section, and $g(y)$ is a geometric mapping factor introduced to map the hydrodynamic pressure

[1]The natural frequencies of a translating wire decreases to $\omega_n' = (1 - V^2m/T)\omega_n$, where ω_n is the natural frequencies of a stationary wire. With $T = 25\,\text{N}$, $m = 1.876 \times 10^{-4}\,\text{kg/m}$, and $V = 10\,\text{m/s}$, which are typical in the industrial wiresaw processes, ω_n' is about 99.9% of ω_n, because $V^2m/T \ll 1$.

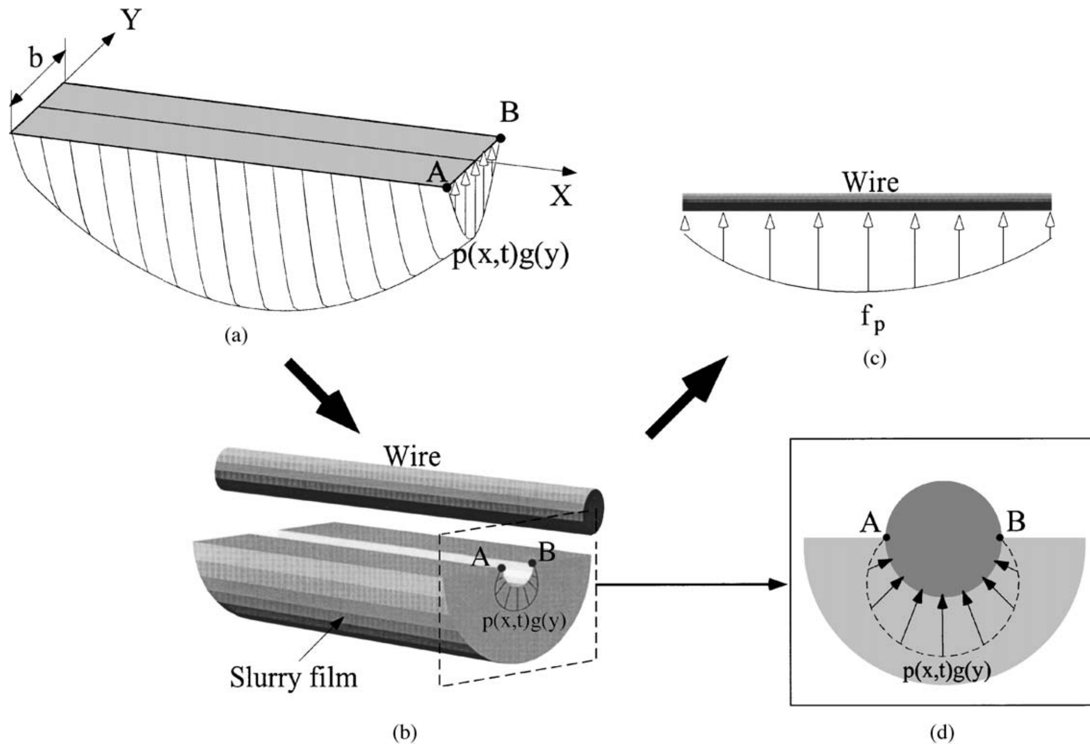

Fig. 3. Procedure of computing the distributed force generated by hydrodynamic pressure in the slurry film. (a) Distribution of hydrodynamic pressure along the flattened lower circumference of the wire cross-sections; (b) distribution of hydrodynamic pressure along the semi-circular lower circumference of the wire cross-sections; (c) distributed force generated by slurry pressure; (d) normal view of pressure distribution along the lower circumference of a wire cross-section.

from the 2D computational domain back to the semi-circular cross-sections of the wire [6]

$$g(y) = \cos\left(\frac{\pi y}{b}\right). \tag{6}$$

Since the transverse motion of the wire is constrained at both ends by wire guides, the boundary conditions for Eq. (2) are

$$U_{\text{tot}}(0, t) = U_{\text{tot}}(L, t) = 0. \tag{7}$$

The slurry flow between the wire and its recess on the ingot is incompressible. From the previous measurements of slurry viscosity, the slurry used in the wiresaw processes is pseudo-plastic, which has shear thinning characteristics [19]. However, the actual behavior of the slurry flow is not markedly different from the Newtonian behavior under high shear rates in the wiresaw processes [6,16,20]. Since the side-leakage has been neglected (see Eq. (5)), the transient Reynold's equation for the incompressible flow is employed to model the hydrodynamic characteristics of the

slurry film [19],

$$\frac{\partial}{\partial x}\left[h(x,t)^3\,\frac{\partial P(x,t)}{\partial x}\right] = 6\mu V\,\frac{\partial h(x,t)}{\partial x} + 12\mu\,\frac{\partial h(x,t)}{\partial t}, \quad (x_1 \leqslant x \leqslant x_2), \tag{8}$$

where μ is the dynamic viscosity of the slurry flow (ranging from tens to thousands *centi poise* in the typical wiresaw processes) and h is the time-varying thickness of the slurry film. The two terms on the right-hand side of Eq. (8) represent a "wedge effect" and a "squeeze film damping" [19], respectively. Both of them are produced by the slurry flow and are transversely acting on the wire. The boundary conditions associated with Eq. (8) are [19]

$$P(x_1,t) = P(x_2,t) = P_{\mathrm{amb}}, \tag{9}$$

where P_{amb} is the ambient pressure.

Comparing with the cutting load exerted by the bowed wire, the external excitation resulting from the multiple contacts between the wire and the abrasive particles (or other solid media in the slurry film) is much smaller under semi-contact and non-contact (floating machining) conditions in the wiresaw processes. Therefore, the vibration amplitude of the wire is also expected to be small compared to the total transverse deflection of the wire. Hence, the slurry film thickness h can be divided into two terms: (1) an equilibrium[2] film thickness, h_0, and (2) a small perturbation (shown as the vibration amplitude of the wire in Fig. 9), $U(x,t) = \varepsilon h(x,t)$, which is equal to the vibration displacement of the wire about its equilibrium position within the contact span. That is,

$$h(x,t) = h_0(x,t) + U(x,t), \quad (x_1 \leqslant x \leqslant x_2). \tag{10}$$

Inserting Eq. (10) into Eq. (8) and combining the resulting expression with Eq. (2), the homogeneous vibration system containing wire–slurry interaction can be linearized [8,9] by striking off the terms containing ε of order higher than one. By keeping all transient terms in the resulting linearized system, we obtain

$$m\,\frac{\partial^2 U(x,t)}{\partial t^2} - T\,\frac{\partial^2 U(x,t)}{\partial x^2} - C_1 p(x,t)[H_{x1}(x) - H_{x2}(x)] = 0, \\ (0 \leqslant x \leqslant L,\, U(0) = U(L) = 0), \tag{11}$$

$$\frac{\partial}{\partial x}\left[h_0(x)^3\,\frac{\partial p(x,t)}{\partial x}\right] = 12\mu\frac{\partial U(x,t)}{\partial t} + 6\mu V\,\frac{\partial U(x,t)}{\partial x} - 3\,\frac{\partial}{\partial x}\left[h_0(x)^2\,\frac{\mathrm{d}P_0(x)}{\mathrm{d}x}\,U(x,t)\right], \\ (x_1 \leqslant x \leqslant x_2, p(x_1) = p(x_2) = 0), \tag{12}$$

where C_1 is a constant depending on the geometry of the cross-sections of the wire (see Eq. (5)). In Eq. (11), $U(x,t) = \varepsilon h(x,t)$ and $p(x,t) = \varepsilon P(x,t)$ are the transient parts in the transverse displacement of the wire and the pressure of the slurry, respectively; i.e.,

$$U(x,t) = U_{\mathrm{tot}}(x,t) - U_0(x), \quad p(x,t) = P(x,t) - P_0(x),$$

[2] Under the rolling-indenting floating machining conditions, the wire is at equilibrium position when the cutting load is balanced by the hydrodynamic pressure inside the slurry flow when there exists no external excitations.

where $U_0(x)$ and $P_0(x)$ are the wire displacement and the slurry pressure when the wire/slurry system is at equilibrium. They have already been studied in Refs. [6,16]. The Galerkin-based discretization and subsequent modal analysis to be presented in the next sections are based on the linear system formed by Eqs. (11) and (12). The forced vibration characteristics of the wire/slurry system are also to be investigated when the wire is subjected to the multi-contact excitation $f(t)$ along the contact span.

2.3. Calculation of the slurry film thickness and pressure at equilibrium

The equilibrium state of the wire/slurry system has been studied in Refs. [6,16]. In these studies, the time-independent form of Eq. (11) and the steady-state 2D Reynold's equation for incompressible fluid (with Swift–Steiber boundary conditions) are employed to model the equilibrium EHD interaction. Numerical schemes formed by incorporating the finite-element method and Newton–Raphson [6] or Inexact Newton GMRES iterations [16,21] are adopted to solve the coupled nonlinear governing equations. They work by minimizing the error in the equilibrium film thickness field. Correspondingly, the discrete equilibrium slurry pressure and film thickness are obtained numerically. These hydrodynamic properties of the slurry film have been studied under various parameter settings. Typical 2D profiles of the equilibrium slurry pressure and film thickness are shown in Fig. 4. These results are similar to those found in Ref. [6]. Some key observations obtained from the study of the equilibrium wire/slurry system are highlighted in the following:

1. The equilibrium slurry pressure does not change drastically along the lower circumferences of the wire cross-sections except near the boundaries of the slurry film, where it suddenly tapers down to zero. Therefore, the equilibrium hydrodynamic behavior of the slurry is close to that of the 1D flow.
2. Convergent channels for the slurry flow, which is along the moving direction of wire, can always be formed, provided that the slicing condition is moderate. Therefore, the profiles of the film thickness and pressure are similar in shape (along the wire moving direction) with different parameter settings.
3. The typical maximum EHD pressure locates near the middle of the contact span. Before reaching its maximum value, the EHD pressure increases rapidly from zero near the inlet (x_1), which is very important in opening a continuous passage for the slurry flow. The increase rate of the EHD pressure becomes a little smaller after the inlet part. Then the pressure increases rapidly again near the middle of the contact span until reaching its maximum value. Afterwards, it decreases smoothly and stays at zero near the exit point x_2.

To facilitate the analysis of the wire/slurry system, the 2D discrete equilibrium pressures and film thicknesses are averaged into 1D forms over the lower half circumferences of the wire cross-sections, respectively. For example, the dimension-reduced equilibrium pressure and film thickness profiles are shown in Fig. 5, which are obtained at different speeds and tensions of the wire (see also Section 4.1.2). In addition, the corresponding 3D profiles of slurry hydrodynamic pressure within boundary layers are plotted in Fig. 6.

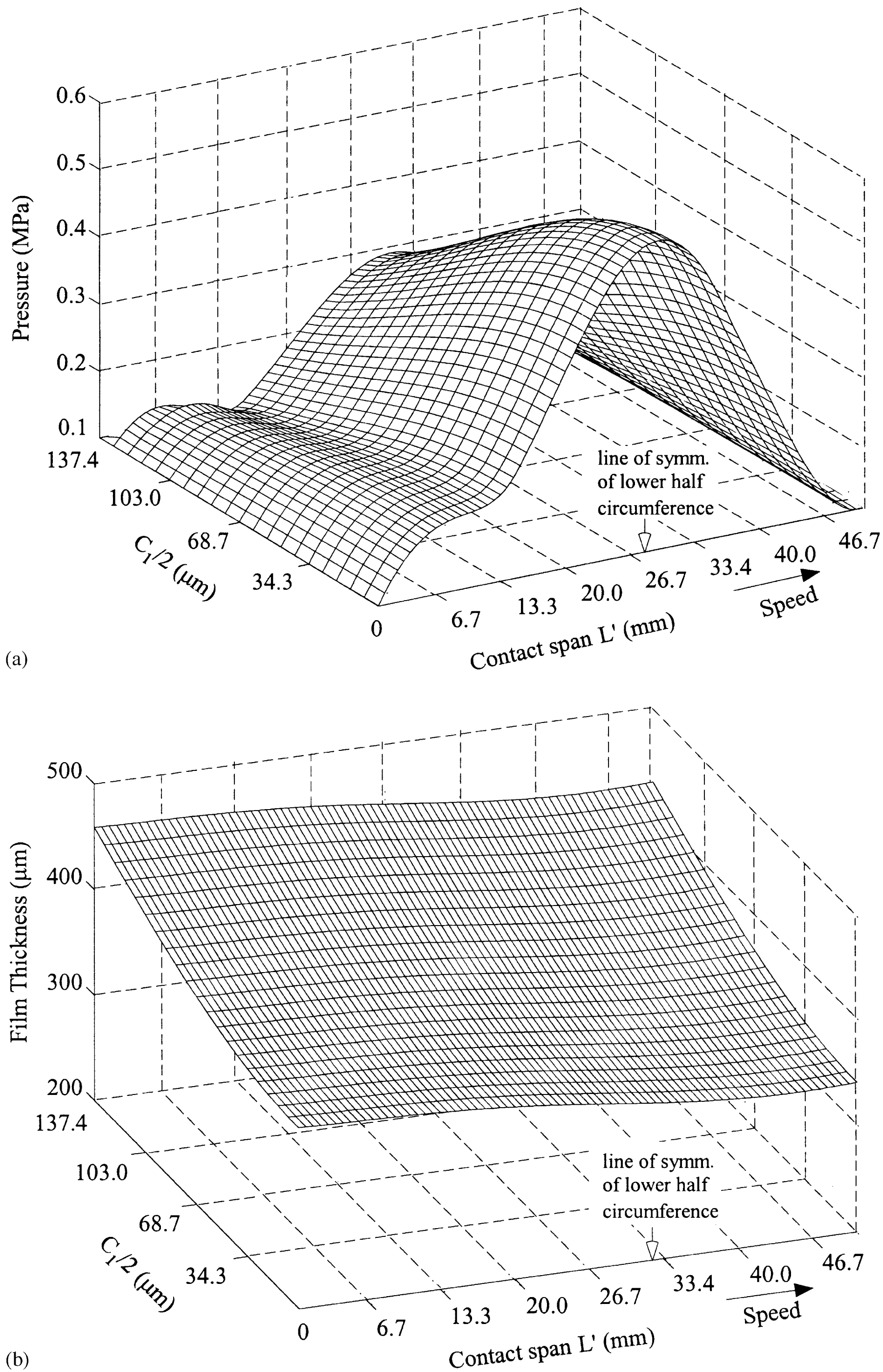

Fig. 4. 2D slurry pressure and film thickness at equilibrium, the results are obtained from FE analysis. Possible minor end effects are neglected. (a) 2D slurry pressure at equilibrium; (b) 2D slurry film thickness at equilibrium. The parameters used in the simulation are: contact span $L' = 50\,\text{mm}$, slurry viscosity $\mu = 5000\,\text{cP}$, wire tension $T = 20\,\text{N}$, wire speed $V = 15\,\text{m/s}$, and wire bow angle $\alpha = 1.2°$.

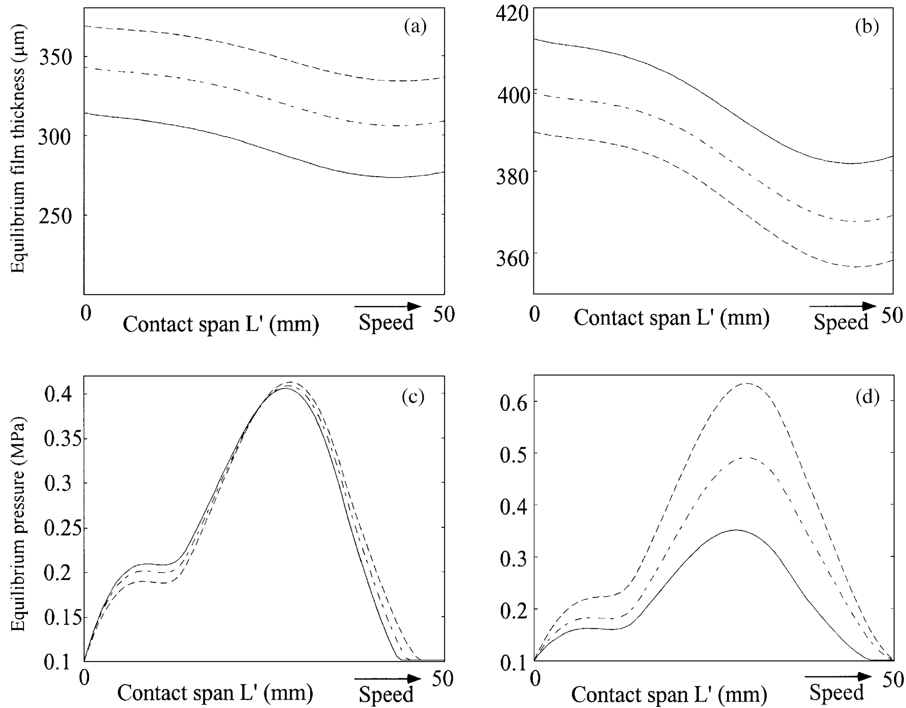

Fig. 5. Dimension-reduced equilibrium film thickness and pressure at different speeds and tensions of the wire. Parameters used in the simulation are the same as those in Section 4.1.2. (a) Thickness of slurry film at speed $V = 10$, 15, 20 m/s and under tension $T = 20$ N. (b) Thickness of slurry film under tension $T = 15$, 25, 35 N and at speed $V = 15$ m/s. (c) Slurry pressure at speed $V = 10$, 15, 20 m/s and under tension $T = 20$ N. (d) Slurry pressure under tension $T = 15$, 25, 35 N and at speed $V = 15$ m/s. For (a) and (c): solid lines represent the cases with $V = 10$ m/s, dashdotted lines represent the cases with $V = 15$ m/s, and dashed lines represent the cases with $V = 20$ m/s. For (b) and (d): solid lines represent the cases under $T = 15$ N, dashdotted lines represent the cases under $T = 25$ N, and dashed lines represent the cases under $T = 35$ N.

3. Model discretization

3.1. Galerkin-based model discretization

Galerkin's method of weighted residuals works by minimizing the error between the actual and the discretized fields. It is fulfilled by considering the error function to be orthogonal to the space defined by the shape functions. Fourier series are common choices of the global shape functions as well as the weighting functions. As to the dynamic wire/slurry system, the vibration displacement $U(x, t)$ of the wire and the transient hydrodynamic pressure $p(x, t)$ of the slurry can be expanded into Fourier series as

$$U(x,t) = \sum_{j=1}^{NU} u_j(t)\phi_j(x), \quad (0 \leqslant x \leqslant L), \tag{13}$$

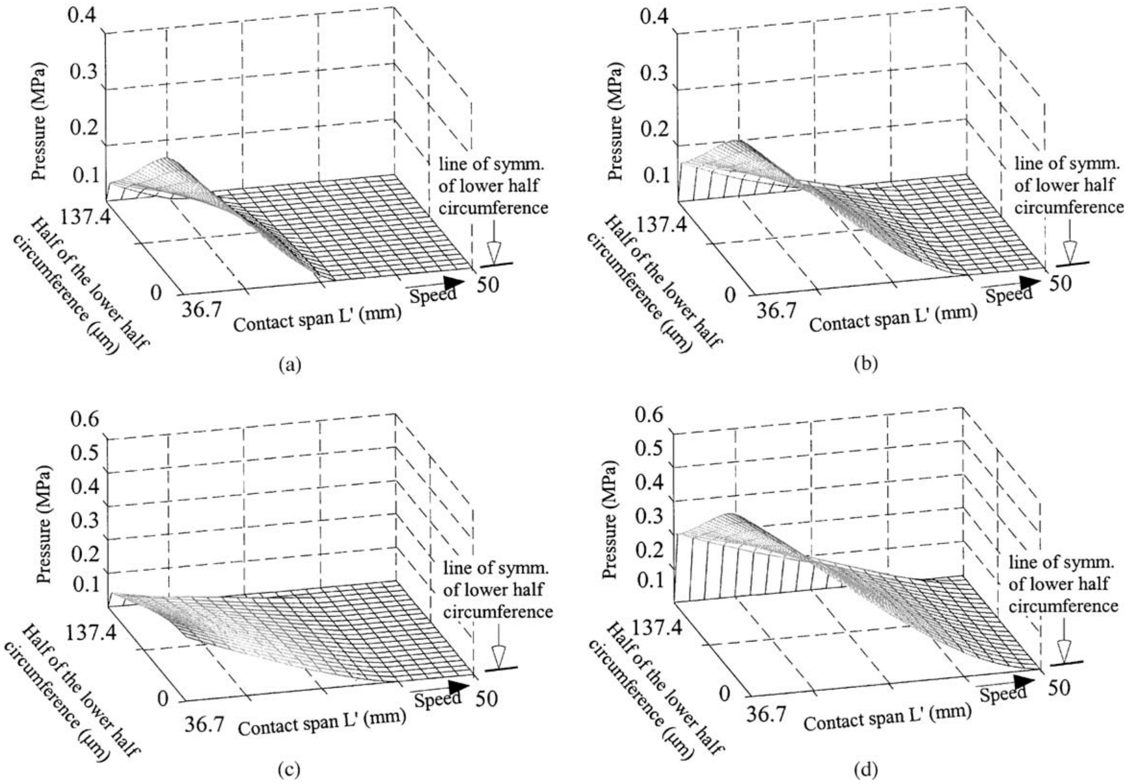

Fig. 6. The 2D profiles of slurry pressure near the boundary region, $36.7\,\mathrm{mm} \leqslant L' \leqslant 50\,\mathrm{mm}$, in Figs. 5 (c) and (d). In this region, the pressure drops to zero at the boundary. (a) Slurry pressure at speed $V = 10\,\mathrm{m/s}$ and under tension $T = 20\,\mathrm{N}$; (b) slurry pressure at speed $V = 15\,\mathrm{m/s}$ and under tension $T = 20\,\mathrm{N}$; (c) slurry pressure under $T = 15\,\mathrm{N}$ and at speed $V = 15\,\mathrm{m/s}$; (d) slurry pressure under $T = 35\,\mathrm{N}$ and at speed $V = 15\,\mathrm{m/s}$.

$$p(x,t)[H_{x_1} - H_{x_2}] = \sum_{j=1}^{NP} r_j(t)\psi_j(x), \quad (x_1 \leqslant x \leqslant x_2), \tag{14}$$

where NU and NP are the number of terms of the Fourier expansions for the wire displacement and the slurry pressure, respectively. The orthogonal and complete shape functions ϕ and ψ are

$$\phi_j = \sin\frac{j\pi x}{L}, \quad \psi_j = \sin\left[\frac{j\pi(x - x_1)}{L'}\right]. \tag{15}$$

Within the contact span L', the distributed external excitation $f(t)$ may also be expanded into Fourier series. However, a more intuitive representation can be obtained by discretizing the external excitation over the entire span of contact, as [7]

$$f(t)[H_{x_1} - H_{x_2}] = \sum_{j=1}^{NF} q_0 \mathrm{e}^{\mathrm{i}\omega_f t}\delta(x_j), \quad x_1 \leqslant x_j \leqslant x_2. \tag{16}$$

Eq. (16) implies that the distributed external excitation is actually resulted from the multi-point contact forces acting on the wire, where NF is the number of these concentrated forces, and $q_0 = f_0 L'/NF$ is the amplitude.

Inserting Eqs. (13), (14) and (16) into Eqs. (11) and (12), the error functions in the wire displacement (EU) and the slurry pressure (EP) fields are

$$EU(x) = \sum_{j=1}^{NU} [m(\phi_j \ddot{u}_j) - T(\phi_j'' u_j)] - C_1 \sum_{j=1}^{NP} \psi_j r_j - \sum_{j=1}^{NF} [\delta(x_j) q_0],$$

$$EP(x) = \sum_{j=1}^{NP} (h_0^3 \psi_j')' r_j - \sum_{j=1}^{NU} [12\mu(\phi_j \dot{u}_j) + 6\mu V(\phi_j' u_j) - 3(h_0^2 P_0' \phi_j)' u_j], \tag{17}$$

where the prime notation "′" denotes the derivatives with respect to x, $\mathrm{d}/\mathrm{d}x$. Following Galerkin's method, the error functions are minimized through rendering them orthogonal to their function spaces:

$$\int_0^L \phi(x)\, EU(x)\, \mathrm{d}x = 0, \quad \int_{x_1}^{x_2} \psi(x)\, EP(x)\, \mathrm{d}x = 0.$$

Therefore, the Galerkin-discretized forced wire/slurry system can be expressed by the weak forms, as

$$\mathbf{M}\ddot{\mathbf{u}} + \mathbf{K}\mathbf{u} - \mathbf{P}\mathbf{r} = \mathbf{F}\mathbf{q}, \quad \mathbf{P}_1\mathbf{r} = \mathbf{C}\dot{\mathbf{u}} + \mathbf{H}\mathbf{u}. \tag{18,19}$$

In Eq. (18), $\mathbf{M}$ is the real diagonal positive-definite mass matrix of dimension $NU \times NU$, $\mathbf{K}$ is the real symmetric stiffness matrix of dimension $NU \times NU$, $\mathbf{P}$ and $\mathbf{F}$ are real $NU \times NP$ and $NU \times NF$ matrices, respectively, $\mathbf{q}$ is the $NF \times 1$ force vector representing the discrete external excitations. In Eq. (19), $\mathbf{C}$ and $\mathbf{H}$ are real $NP \times NU$ matrices, $\mathbf{P}_1$ is a real $NP \times NP$ non-symmetric matrices. The elements of these matrices (vectors) are

$$M(i,j) = m \int_0^L \phi_i \phi_j \, \mathrm{d}x; \quad (i,j = 1, \ldots, NU),$$

$$K(i,j) = T \int_0^L \phi_i' \phi_j' \, \mathrm{d}x; \quad (i,j = 1, \ldots, NU),$$

$$P(i,j) = C_1 \int_{x_1}^{x_2} \phi_i \psi_j \, \mathrm{d}x; \quad (i = 1, \ldots, NU;\ j = 1, \ldots, NP),$$

$$F(i,j) = \int_{x_1}^{x_2} \phi_i \delta(x_j) \, \mathrm{d}x; \quad (i = 1, \ldots, NU;\ j = 1, \ldots, NF),$$

$$q(j) = q_0 \mathrm{e}^{\mathrm{i}\omega_f t}; \quad (j = 1, \ldots, NF),$$

$$C(i,j) = 12\mu \int_{x_1}^{x_2} \psi_i \phi_j \, \mathrm{d}x; \quad (i = 1, \ldots, NP;\ j = 1, \ldots, NU),$$

$$H(i,j) = -6\mu V \int_{x_1}^{x_2} \psi_i' \phi_j \, \mathrm{d}x + 3 \int_{x_1}^{x_2} h_0^2 P_0' \phi_j \psi_i' \, \mathrm{d}x; \quad (i = 1, \ldots, NP; \; j = 1, \ldots, NU),$$

$$P_1(i,j) = -\int_{x_1}^{x_2} h_0^3 \psi_j' \psi_i' \, \mathrm{d}x; \quad (i,j = 1, \ldots, NP),$$

where the $\mathbf{P}_1$ matrix and the second part of the $\mathbf{H}$ matrix are obtained through integration over the nodal points x_n ($x_1 \leqslant x_n \leqslant x_2$) of the discrete equilibrium slurry pressure and film thickness. Euler's rule is applied to evaluate the corresponding derivatives. Eqs. (18) and (19) can be combined to yield the linear system describing the vibration characteristics of the wire/slurry system:

$$\mathbf{M}\ddot{\mathbf{u}} + \mathbf{C}^{*}\dot{\mathbf{u}} + (\mathbf{K} + \mathbf{H}^{*})\mathbf{u} = \mathbf{F}\mathbf{q}. \tag{20}$$

In Eq. (20), $\mathbf{C}^{*} = -\mathbf{P}\mathbf{P}_1^{-1}\mathbf{C}$ is a $NU \times NU$ real non-symmetric matrix representing the slurry damping, and $\mathbf{H}^{*} = -\mathbf{P}\mathbf{P}_1^{-1}\mathbf{H}$ is a $NU \times NU$ real non-symmetric matrix representing the added stiffness of the wire mainly due to the wedge effect. These two terms are newly introduced matrices in the investigation of the dynamically coupled wire/slurry system of the wiresawing processes.

The slurry damping acting on the wire comes from the elasto-hydrodynamic squeeze film effect. As the wire vibrates transversely, the slurry film, which is trapped between wire and ingot recess, is squeezed, hence exerts damping force on the wire. Therefore, the slurry damping is of the viscous type. In the following simulation in Section 4, typical values of the elements in the damping matrix $\mathbf{C}^{*}$ have magnitude ranges from 0 to 10^3 kg/s.

Eq. (20) represents a general non-conservative system with asymmetric matrices [22], which results in non-symmetric vibration characteristics induced by the coupling of the wire and the slurry flow. To our best knowledge, this system asymmetry in the wiresaw slicing process has not been modeled and studied in detail before.

3.2. Verification of the Galerkin-discretized model

According to Ref. [22], the closed-form solution is generally not available for such non-conservative system as described by Eqs. (11) and (12). Therefore, the numerical scheme of finite element (FE) semi-discretization is employed to verify the Galerkin-discretized model. First, the original system given by Eqs. (11) and (12) is discretized into piecewise linear-interpolated elements. Next, the temporal behavior of such FE approximation is directly integrated by the one-step Newmark's predictor–corrector method. The reason for choosing the Newmark's method is because of its unconditional stable property [17]. Both models have been tested by the same randomly selected parameters, with a wire of diameter 175 μm and the mass per unit length 0.1876 g/m. The wire length is $L = 300$ mm. Here, we use the slurry comprised of Glycol or Ecocool carrier and F400 SiC abrasive grits with an effective viscosity of 10 cP (centi-poise). The equilibrium film thickness h_0 of the slurry is set as constant at 150 μm over the contact span of 10 mm. This randomly selected film thickness is in the order of the slurry film thickness obtained from Refs. [6,16] and relatively thin corresponding to the low slurry viscosity. These relatively low dynamic viscosity and uniform film thickness are chosen primarily to reduce the computation effort in the direct time integration. Other choices are also used in the simulation with similar results. The harmonic external excitation is assumed to be sinusoidal. Other process parameters

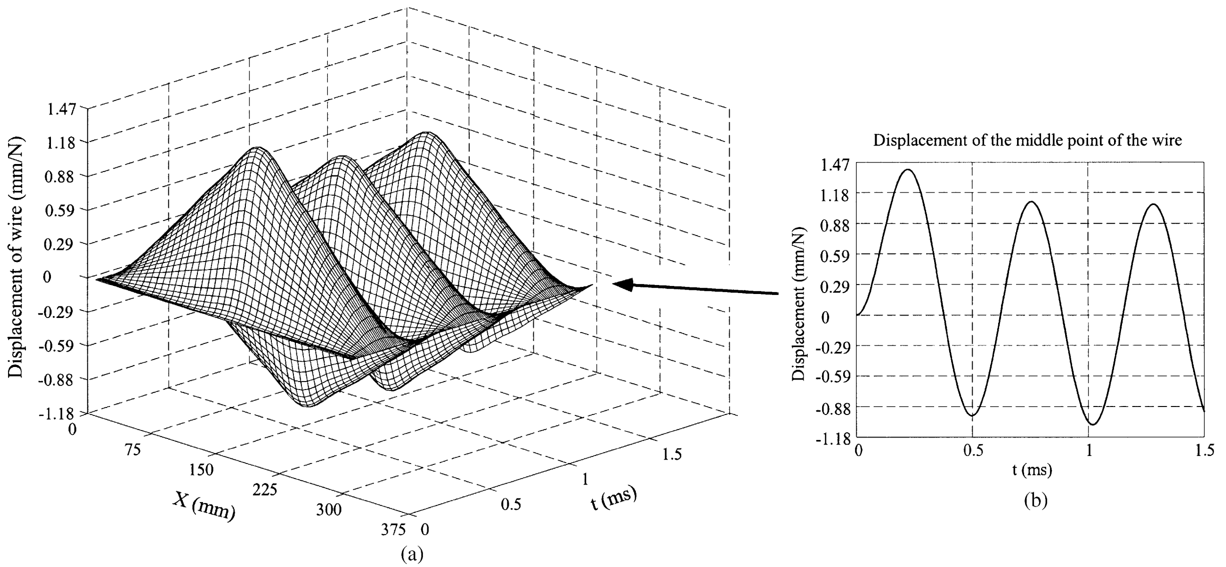

Fig. 7. Time domain forced vibration response of wire calculated from the Galerkin-discretized model. The transverse displacement of the wire is normalized with respect to the magnitude of external excitation, $U(f_0 L')$. (a) Vibration displacement of the whole wire; (b) vibration displacement of the middle point of the wire. Parameters used in the simulation are: wire tension $T = 25\,\mathrm{N}$, wire speed $V = 10\,\mathrm{m/s}$, wire length $L = 300\,\mathrm{mm}$, contact span $L' = 10\,\mathrm{mm}$, slurry viscosity $\mu = 10\,\mathrm{cP}$, and the frequency of external excitation $\omega_f = 1200\,\mathrm{rad/s}$.

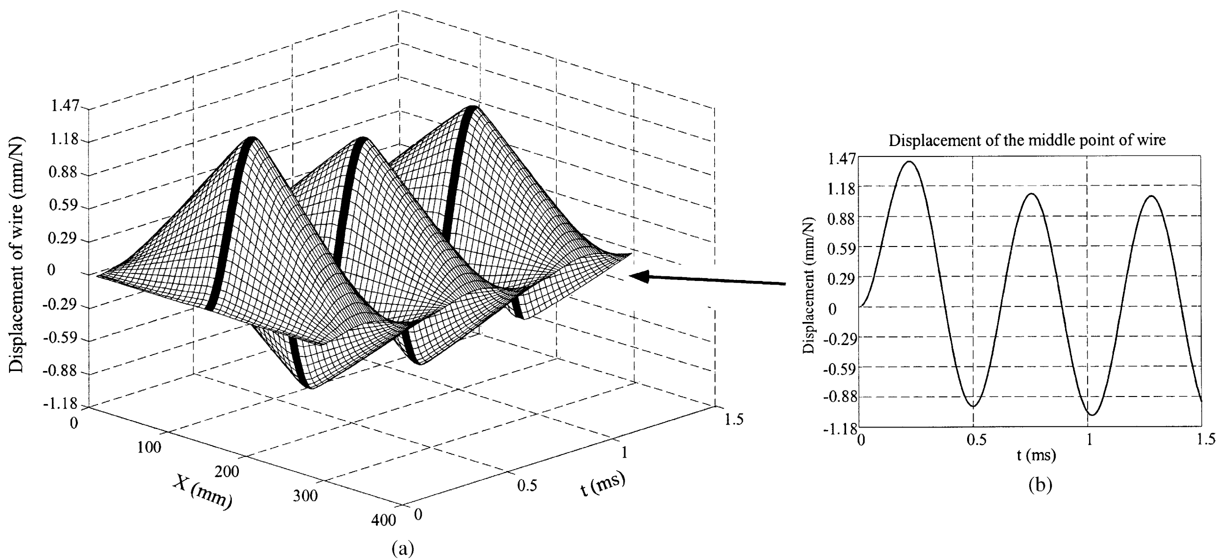

Fig. 8. Time domain forced vibration response of wire calculated from direct-time integration by Newmark's method. As illustrated in the figure, finer elements are assigned in the middle of the wire, in accordance with the contact span. The transverse displacement of the wire is normalized in the same way as that in Fig. 7. (a) Vibration displacement of the whole wire; (b) vibration displacement of the middle point of the wire. Parameters used in the simulation are the same as in Fig. 7.

are indicated in Figs. 7 and 8. The responses of the forced vibration of wire are calculated in the time domain by applying both models (Galerkin-discretized model and FE semi-discretized model) under zero initial conditions. The vibration displacements of the wire are plotted in 3D plots against the X-axis and the time in Figs. 7 and 8, respectively. These two figures show that the vibration responses of wire obtained from these two models are reasonably close to each other, even though finer elements are assigned in the middle of the wire in Fig. 8.

Although the numerical scheme of the direct-time integration can also yield good results in the time domain, there are many disadvantages associated with it. The major ones are: (1) the computational cost is unaffordable in computing large data sets; and (2) it is not physically intuitive in the understanding of the system.

Therefore, we employ modal analysis in the study of the Galerkin-discretized model, which will be presented in the next section.

4. Modal analysis

General non-conservative systems, as described by Eq. (20), admit complex eigenvalue solutions. Casting Eq. (20) into the state-space form, we have

$$\dot{\mathbf{v}}(t) = \mathbf{A}\mathbf{v}(t) + \mathbf{B}\mathbf{q}. \tag{21}$$

In Eq. (21), $\mathbf{v}(t) = [\mathbf{u}(t)^{\mathrm{T}}\dot{\mathbf{u}}(t)^{\mathrm{T}}]^{\mathrm{T}}$ is the augmented state vector. The system matrix $\mathbf{A}$ of dimension $2NU \times 2NU$ is real and non-symmetric. The dynamic characteristics of the wire/slurry system are determined by the dual eigenvalue solution [22] of this system matrix $\mathbf{A}$.

From the eigenanalysis of the dynamic wire/slurry system described by Eqs. (20) and (21), the key results are highlighted in the following:

1. The eigensolutions of Eq. (20) consist of complex eigenvalues and real eigenvalues (as shown in Table 1 and Fig. 13). The complex conjugate eigenvalues contain the vibration modes of the wire/slurry system, which are described by the damped frequencies and the effective dampings of these modes. The real eigenvalues correspond to the overdamped high-frequency modes [23]. The system vibration responses associated with these overdamped modes are merely affected by the excitation frequency. The contribution of these overdamped modes to the vibration amplitude of the wire

Table 1
First four underdamped modes of vibration at different contact spans

Contact span L'	30 mm	50 mm	70 mm	90 mm
1st underdamped mode	$-38.6 \pm 4364i$	$-49.7 \pm 4549i$	$-51.4 \pm 4757i$	$-55.5 \pm 4987i$
2nd underdamped mode	$-9.3 \pm 4374i$	$-14.0 \pm 4556i$	$-15.4 \pm 4761i$	$-17.5 \pm 4988i$
3rd underdamped mode	$-73.6 \pm 8747i$	$-74.0 \pm 9127i$	$-79.3 \pm 9535i$	$-86.9 \pm 10000i$
4th underdamped mode	$-24.8 \pm 8761i$	$-41.8 \pm 9128i$	$-45.2 \pm 9546i$	$-46.3 \pm 9999i$

The real part of any eigenvalue decreases when the contact span becomes longer, which indicates the effective damping gets larger at longer contact span. The damped frequencies of modes $(2i-1)$ and $(2i)$ are close to each other, because the ingot is placed at the mid-span of the wire.

becomes progressively smaller when the excitation frequency increases from zero [23]: When the harmonic excitation is a cosine signal, the vibration amplitude of the wire decreases monotonically as the excitation frequency increases from zero; whereas, when the system is subject to a sinusoidal excitation, the vibration amplitude of the wire experiences an abrupt shoot-up from zero amplitude in a narrow band near zero frequency, then decreases monotonically. Therefore, these overdamped mode will not lead to resonance-type phenomena (see Fig. 14). However, the low-frequency response of the system is determined by these real eigenvalues.

2. The damped frequencies of modes $(2i-1)$ and $(2i)$, with $i\geqslant 1$, are nearly identical to each other. This phenomenon has been observed and discussed in the study of tape/head system in Ref. [9]. If the wire vibrates without interacting with slurry, a node (or anti-node) of its $j=2i$ (or $j=2i-1$) mode (which is ϕ_j; see Eq. (13)) will be located at the mid point of the wire. With the slurry/wire interaction, the damping effect of the slurry is somewhat similar to the case when the wire is constrained from the transverse displacement at the middle point, as illustrated in Figs. 9 and 10. In the context of wiresawing process, therefore, the damped frequencies of the wire/slurry system would be repeated at the wire's even natural frequencies.

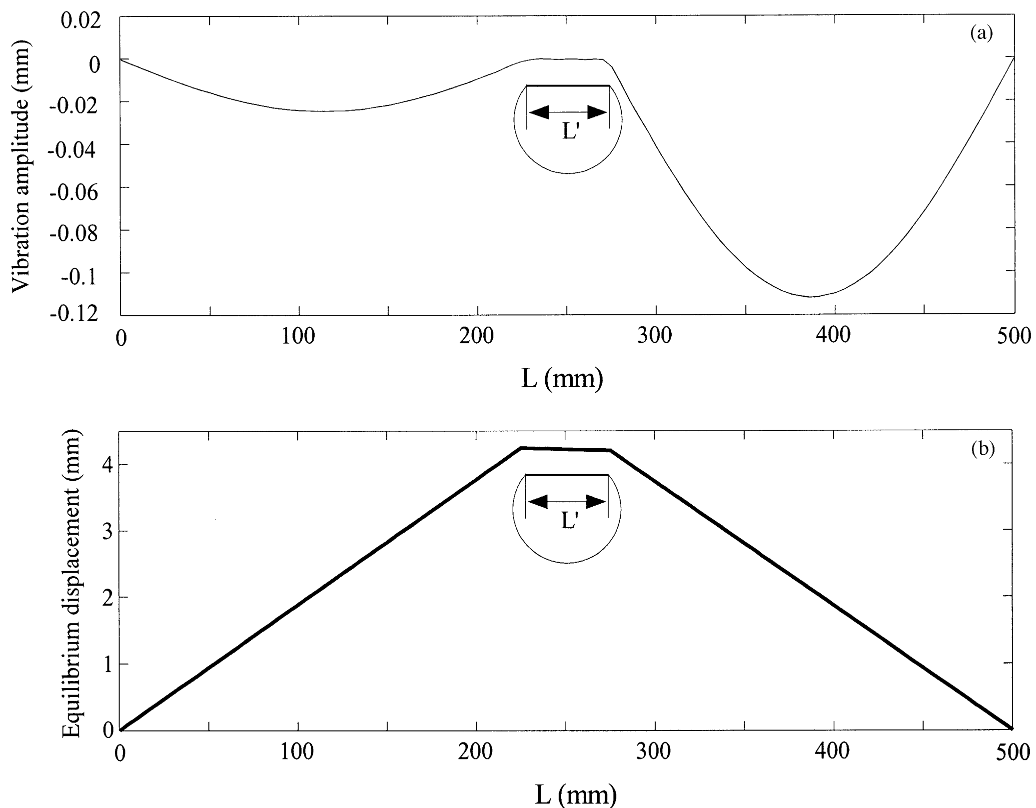

Fig. 9. The vibration amplitude and the equilibrium displacement of the wire. The parameters are the same as those in Fig. 10. The vibration amplitude of the wire is found to be much smaller than the wire deflection at equilibrium, which validates the small perturbation assumption in the previous linearization procedure. (a) Vibration amplitude of the wire; (b) deflection of the wire at equilibrium.

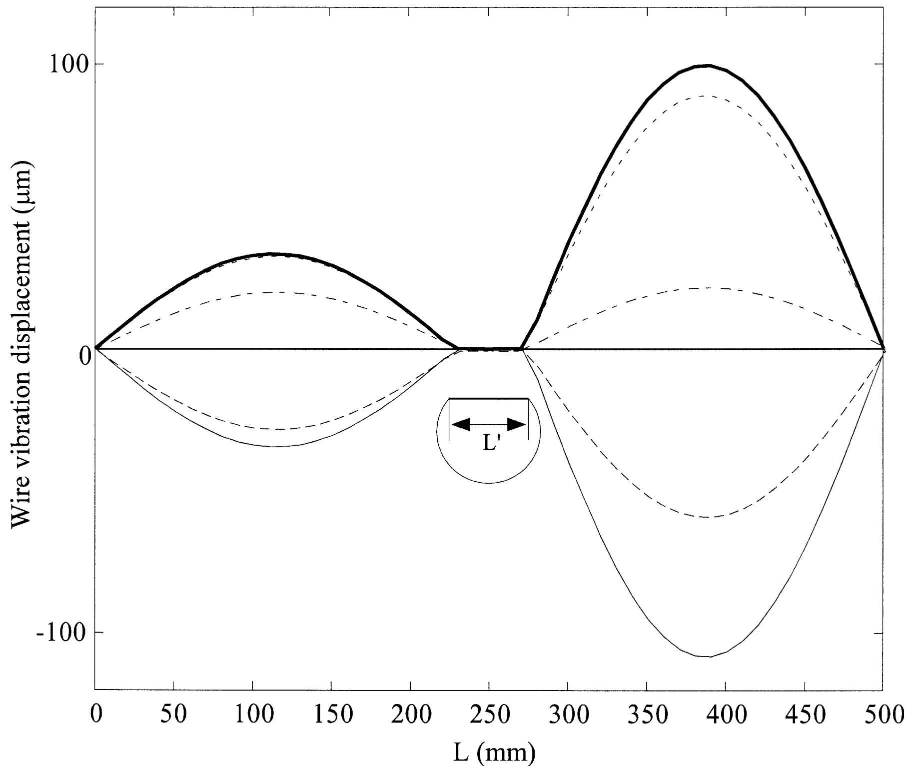

Fig. 10. Vibration displacement of the wire as a function of time. The ingot is located at the middle part of the wire. The wire/slurry interaction occurs within the contact span L', as shown. Parameters used in the simulation are: contact span $L' = 50\,\text{mm}$, speed $V = 10\,\text{m/s}$, tension $T = 20\,\text{N}$, slurry viscosity $\mu = 2500\,\text{cP}$, wire bow angle $\alpha = 1.0°$, the frequency of external excitation $\omega_f = 4558.7\,\text{rad/s}$, and the amplitude of external excitation $f_0 = 6.98\,\text{N/m}$. In the figure, the wire has zero initial displacement. The thick solid line represents the vibration displacement of the wire after 0.1 s. The thin solid line represents the wire displacement after 0.2 s. The dotted line represents the wire displacement after 0.3 s, the dashed and the dashdotted lines represent the wire displacements after 0.4 and 0.5 s, respectively.

3. From the above discussions, the damped frequencies of $(2i-1)$ and $(2i)$ modes of the wire/slurry system are higher than the natural frequency of the $(2i)$ mode of the wire. This is because the contact span occupies a part of the wire length. In the case presented in Section 4.1.1, for example, the second natural frequency of the wire is about 4145 rad/s. The damped frequencies of the corresponding wire/slurry system are higher, ranging from 4364 to 4988 rad/s depending on contact spans, as shown in Table 1.
4. System eigenvalues always possess negative real parts, which indicates that the equilibrium positions of the wire/slurry system are asymptotically stable with typical configurations in the wiresawing process. This conclusion can be extended to the original nonlinear wire/slurry system since the linearized system possesses *significant behavior* [22]. Therefore, the system stability is guaranteed for all practical concerns.

A typical profile of the vibration amplitude of the wire is plotted in Fig. 9 with the comparison of the equilibrium displacement of wire. In this case, the wire is subjected to a sinusoidal

Table 2
First two underdamped vibration modes at different wire speeds, $V = 10$, 12.5, 15, and 20 m/s

Wire speed V (m/s)	10	12.5	15	20
1st underdamped mode	$-41.9 \pm 4559i$	$-45.6 \pm 4557i$	$-49.4 \pm 4553i$	$-56.3 \pm 4551i$
2nd underdamped mode	$-17.4 \pm 4563i$	$-14.8 \pm 4562i$	$-12.9 \pm 4560i$	$-9.2 \pm 4558i$

excitation (Im[$f(t)$] in Eq. (4)) with ω_f equal to the first damped frequency of the system (see Table 2). Fig. 10 shows the vibration displacements of the wire with respect to time. The process parameters used in the simulation are shown in Fig. 10. The magnitude of the external excitation is calculated through the following equation:

$$N_n = 2T \sin \alpha = C_2 L' P_{\text{avg}} \quad \text{and} \quad f_0 = \beta N_n / L'. \tag{22,23}$$

In Eqs. (22) and (23), N_n is the nominal cutting force generated from the bow angle and tension of the wire, P_{avg} is the equilibrium hydrodynamic pressure generated in the slurry film, which is averaged along the contact span; C_2 is a constant depending on the geometry of the cross-section of the wire, and β is the ratio between the magnitude of the external disturbance force and the nominal cutting load. Assuming the magnitude of the external excitation accounts for 10% of the total nominal cutting force ($\beta = 0.1$), the vibration amplitude of the wire is found to be much smaller than the wire deflection at equilibrium, as shown in Fig. 9. This validates the small perturbation assumption in the previous linearization procedure.

4.1. *Parametric studies of the vibration of wire in slurry wiresawing processes*

By applying corresponding eigenanalysis to the Galerkin-discretized model, parametric studies have been carried out numerically to investigate the vibration of wire in the slurry wiresawing processes. The process parameters used in the following simulations are based on the typical configurations in the silicon wafer wiresaw slicing processes. The mass density of the wire is 0.1836 g/m (plain carbon steel wire). The length of the wire is $L = 500$ mm (E400SD series wiresaw), with the slurry being a mixture of F400 green silicon carbide abrasives and Glycol or Ecocool-base carrier at various mixing ratios.

Important parameters affecting the wiresaw processes include: (1) the contact span L'; (2) the properties of wire: wire speed V, wire tension T, and wire bow angle α; (3) the dynamic viscosity of the slurry μ. Numerical simulation has been conducted to investigate the effects of these process parameters on the dynamics of the wire/slurry system. Within the practical ranges of these process parameters, the vibration characteristics of the wire are studied by varying the range of each individual parameter while keeping other parameters constant. In the following subsections, studies on the contact span, speed and tension of wire, bow angle of wire, and slurry viscosity are presented.

4.1.1. *Contact span*

In slicing cylindrical semi-conductor boules, it is sometimes observed that high roughness can exist in the upper and lower parts of a wiresaw-sliced wafer at shorter contact spans, as shown in

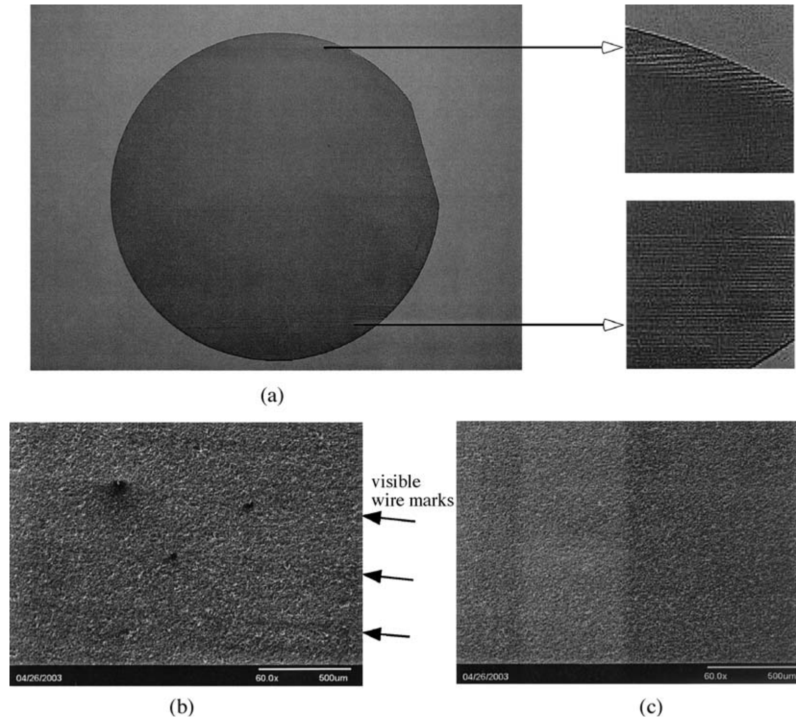

Fig. 11. Wiresaw sliced 5" Si wafer (⟨111⟩ n-type). (a) Large surface roughness is visible at the upper and lower portions of the wafer corresponding to the engaging and exiting parts of the slicing process. (b) SEM photo of a small area at contact span $L' = 45\,\text{mm}$. Comparing with (c): (1) there are more abrasive grits remain indented on the wafer surface; (2) the surface crack pits are larger and coarser; (3) visible wire marks indicating brutal cutting conditions had occurred. (c) SEM photo of a small area at contact span $L' = 125\,\text{mm}$. The surface, under the same scale as in (b), has a much better surface finish.

Fig. 11. The surface roughness of the same wafer is smaller elsewhere. Such defects are highly undesirable in the industrial wiresaw processes since additional lapping will be required in the subsequent processing. In addition, there is a corresponding higher risk of wire breakage when this occurs.

A wiresaw-sliced 5" single-crystalline silicon wafer is shown in Fig. 11(a) to illustrate such characteristics. As indicated by the zoom-in views, visible rough wire marks can be seen with naked eyes. To further study the surface morphology, scanning electron microscope (SEM) photos were taken at small areas located at the contact spans $L' = 45\,\text{mm}$ (upper part of the wafer surface) and $L' = 125\,\text{mm}$ (towards the middle of the wafer surface), respectively. They are shown in Figs. 11(b) and (c). It can be readily seen from these two figures that poor surface finish is produced on this wafer when the contact span is shorter. Parallel wire marks and rougher surface are probably caused by very thin or intermittently broken slurry film, resulting in ploughing instead of the rolling-indenting process [4,6,16]. The SEM photos taken in the same scale show more fractures, larger pits, and surface irregularities in Fig. 11(b) than Fig. 11(c).

Average surface roughness (R_a) values are measured using the *XP-2* Stylus Profiler. The average roughness R_a is calculated from the arithmetic average method, defined as

$$R_a = \sum_{i=1}^{n} \frac{|y_i|}{n}, \tag{24}$$

where y_i is the vertical deviation from the nominal surface at point i, and n is the number of points along a specified distance within which the deviations are measured.

Measurements were taken along 2 mm traces perpendicular to the wire marks at the contact spans of 45, 80, 100 and 125 mm. At every contact span, five measurements separated uniformly by 5 mm distance were taken along the direction of the wire mark. The mean and the corresponding standard deviation of measured R_a values are plotted in Fig. 12 with respect to the different values of the contact spans. The results indicate that the surface roughness decreases continuously with the expansion of the contact span. More importantly, there is a significant reduction in the standard deviation when the contact span is increased from 45 to 80 mm and higher.

One possible reason of such surface roughness is the quick fluctuation of material removal rate (MRR). With normal floating machining environment and rolling-indenting mechanism in the typical wiresawing processes, the MRR is mainly determined by the hydrodynamic pressure developed in the slurry flow, and the thickness of the slurry film [6,16].

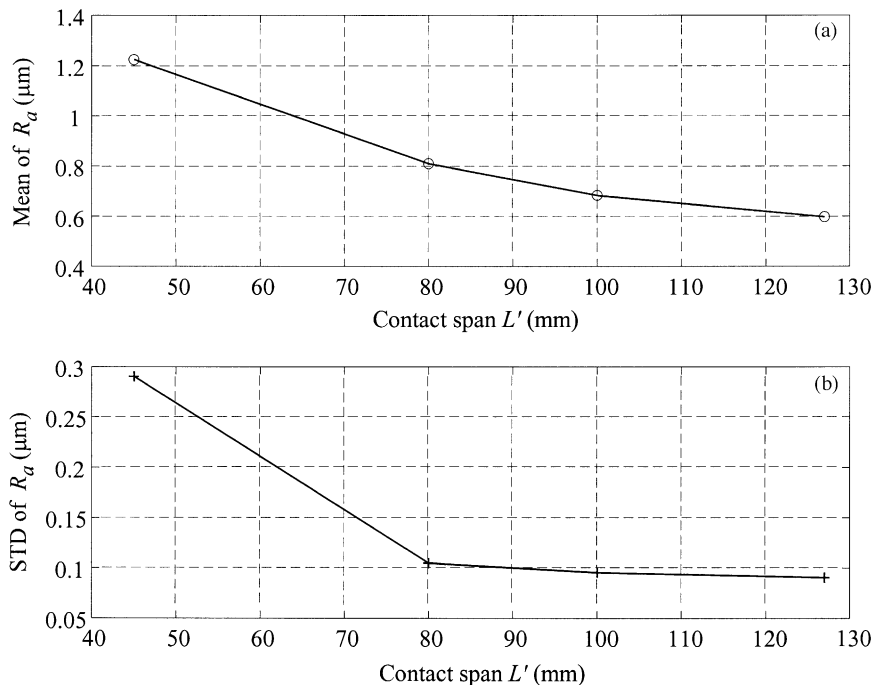

Fig. 12. The mean values and the standard deviations (STD) of the measured surface roughness R_a along different contact spans at $L' = 45$, 80, 100, and 125 mm. (a) Mean values of the measured surface roughness; (b) STD of the measured surface roughness.

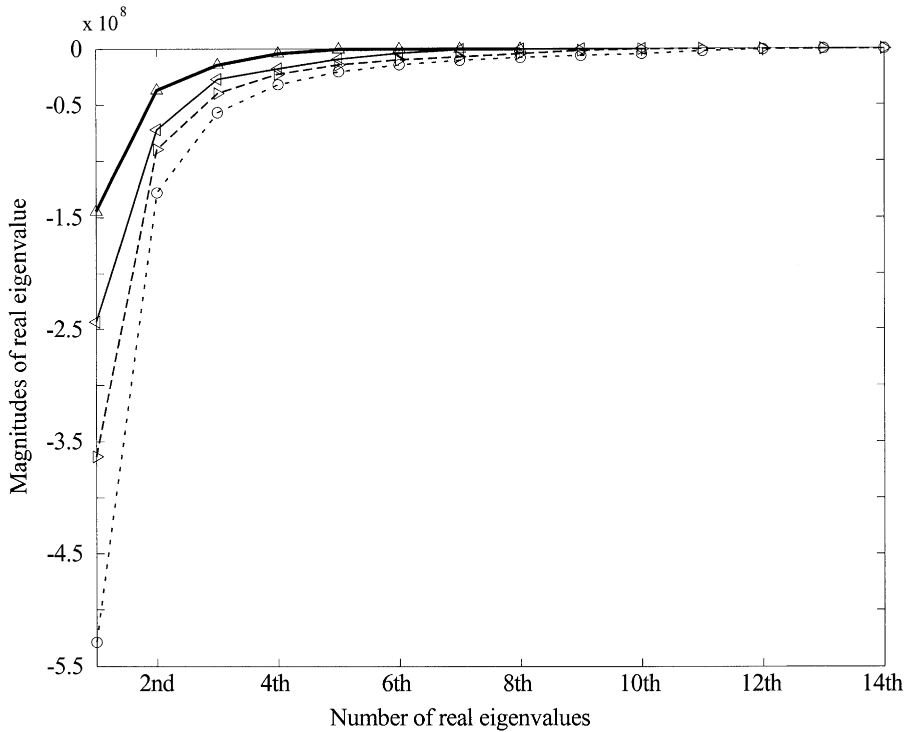

Fig. 13. Real eigenvalues of the wire/slurry system at the contact spans of $L' = 30$, 50, 70, and 90 mm. Parameters used in the simulation are: speed $V = 15\,\mathrm{m/s}$, tension $T = 20\,\mathrm{N}$, slurry viscosity $\mu = 4500\,\mathrm{cP}$, wire bow angle $\alpha = 1.2°$, $NU = NP = 60$, and $NF = 100$. In the figure, the thick solid line connects the 8 real eigenvalues (upward triangles) at contact span $L' = 30\,\mathrm{mm}$. The thin solid line connects the 10 real eigenvalues (left triangles) at contact span $L' = 50\,\mathrm{mm}$. The dashed line connects the 14 real eigenvalues (right triangles) at contact span $L' = 70\,\mathrm{mm}$, and the dotted line connects the 14 real eigenvalues (circles) at contact span $L' = 90\,\mathrm{mm}$.

It can be expressed as

$$\mathrm{MRR} = \mu V^2 \frac{P}{h^2}, \tag{25}$$

where MRR is the material removal rate, P is the hydrodynamic pressure, and h is the thickness of the slurry film. With other process parameters fixed at a certain contact span, the hydrodynamic pressure and the film thickness only fluctuate when the wire vibrates, as shown in Eqs. (10) and (12).

Modal analysis was implemented to study the vibration characteristics of the wire/slurry system at contact spans $L' = 30$, 50, 70, and 90 mm. The real eigenvalues of the system at these contact spans are plotted in Fig. 13, which correspond to the overdamped modes of the system (see Section 4). The first four vibration modes at these contact spans are tabulated in Table 1. In Fig. 14, the maximum vibration amplitude of the wire (which is taken from the point with the largest amplitude on the wire) is plotted against the excitation frequency at different contact spans. In the simulation, the external excitation is assumed to be sinusoidal.

When the excitation frequency is low, the vibration amplitude of the wire decreases as the excitation frequency increases, as shown in Fig. 14. This is because the contribution of the

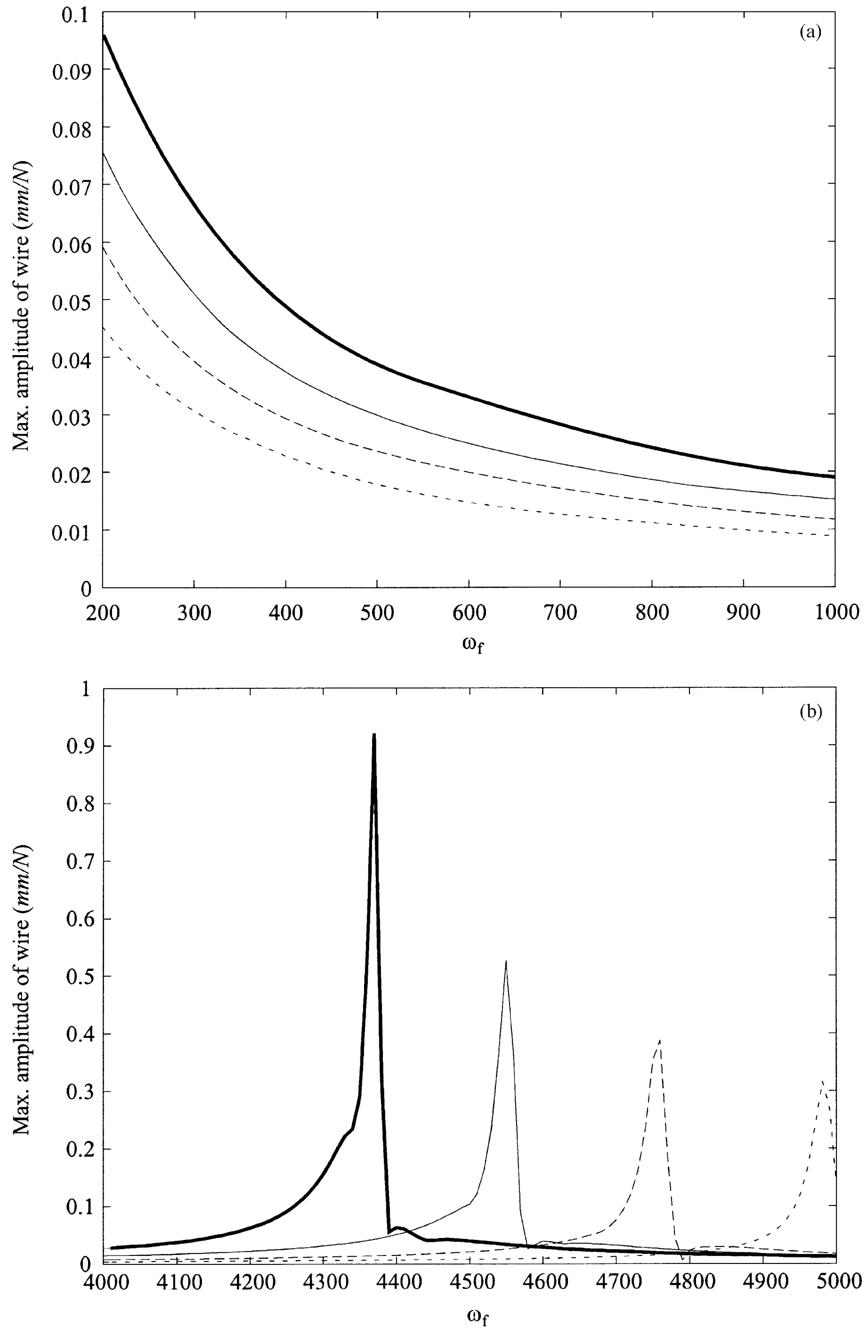

Fig. 14. Maximum vibration amplitudes of the wire at contact spans of $L' = 30$, 50, 70, and 90 mm. The vibration response is studied when the wire is subject to excitations with frequencies (a) near zero, and (b) near the first damped frequency of the system (see Section 4.1.1), respectively. The parameters used in the simulation are the same as in Fig. 13. In the figures, the thick solid lines represent the maximum vibration amplitudes at contact span $L' = 30$ mm. The thin solid lines represent the maximum amplitudes at contact span $L' = 50$ mm. The dashed and dotted lines represent the maximum amplitudes at contact spans $L' = 70$ mm and $L' = 90$ mm, respectively.

overdamped modes decreases as the excitation frequency becomes higher. Afterwards, the system experiences resonance near the first damped frequency. There are two resonance peaks at this frequency region, which is due to the fact that the second damped frequency is very close to the first damped frequency of the system, as shown in Table 1. Since the effective damping is proportional to the magnitude of the real part of the complex eigenvalue, Figs. 13 and 14, and Table 1 indicate that the effective damping of any vibration mode increases with the expansion of the contact span. Correspondingly, the maximum vibration amplitude of the wire decreases at larger contact span, as shown in Fig. 14. Table 1 and Fig. 14 also show that the damped frequencies of the wire/slurry system increase as the contact span becomes larger, which was discussed earlier in this section.

From these simulation results, the shorter contact span produces larger vibration amplitude of the wire. When this is coupled with the potential collapse of the hydrodynamic slurry film [6,16], poor surface finish is produced. This is in accordance with the change in the surface roughness shown in Figs. 11 and 12. Therefore, in order to obtain uniform, low surface roughness of wiresaw-sliced wafers and to minimize the vibration-induced differential saw damage, the process parameters should be controlled adaptively at different contact spans. In industry, such adjustment of process parameters is done by manually assigning values to the important process parameters in a PLC-based controller, such as the feed rate and the wire tension. The methodology developed in this paper can be used to generate optimal profiles of the feed rate corresponding to the bow angle of the wire and the wire tension. An example of adaptively controlling these process parameters in the slicing of 300 mm wafers is presented in Section 5.

4.1.2. Speed and tension of the wire

The speed of wire is normally kept in the range of 10–15 m/s in the industrial wiresawing processes. Within this speed range, it has been found that the change of wire speed does not have much effect on the vibration characteristics of the wire [7]. However, wire speed is very important in establishing and maintaining a hydrodynamic floating machining environment in slurry wiresawing. Simulation has been conducted at different wire speeds ranging from 10 to 20 m/s. In Fig. 15, the maximum vibration amplitude of the wire is plotted against the excitation frequency. Table 2 shows the first two vibration modes of the system under different speeds of $V = 10$, 12.5, 15, and 20 m/s.

From Fig. 15 and Table 2, a few observations are in order:

1. As to the system eigenvalues corresponding to the first two vibration modes, the eigenvalue with larger real part plays a more important role (the second mode in Table 2) in affecting the vibration amplitude of the wire as the excitation frequency approaches the first damped frequency. As shown in Table 2, the effective damping of the second mode decreases when the wire speed becomes higher. Therefore, the maximum vibration amplitude of the wire increases with the wire speed within this frequency region, as shown in Fig. 15.
2. The damped frequencies of the system decrease slightly when the wire speed increases. However, such variation is insignificant due to the limited range of wire speeds[3] used in the industrial wiresaw processes.

[3]Practical wire speeds used in industrial wiresaws are well below the critical speed for instability, i.e., $V \ll V_{cr}$ [7].

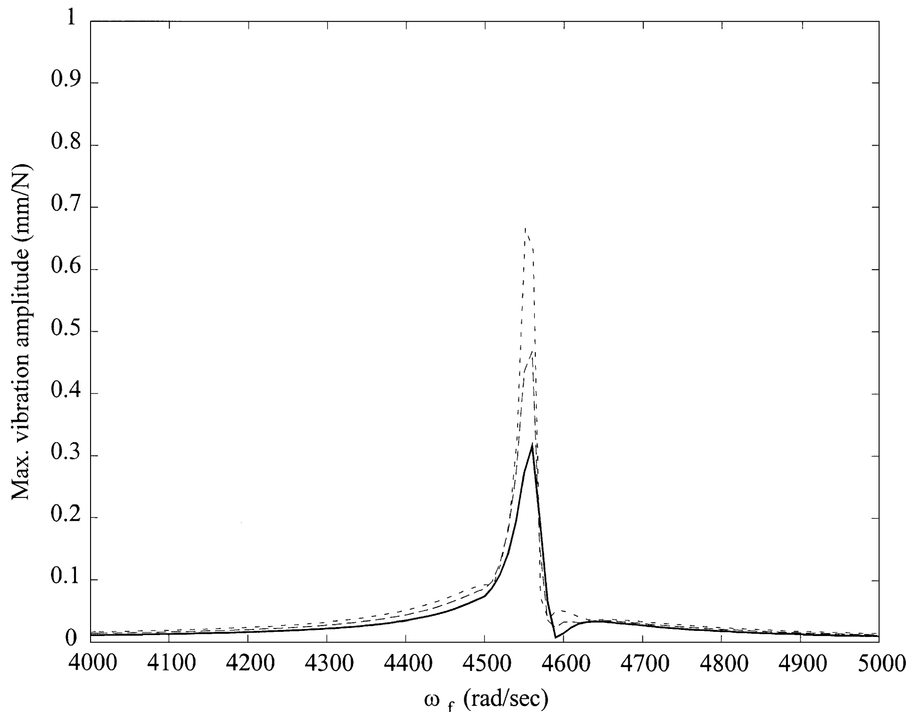

Fig. 15. Maximum vibration amplitudes under different excitation frequencies at $V = 10$, 15, and 20 m/s. The vibration amplitude of the wire increases at higher speed of the wire. The damped frequencies decrease a small amount at higher speed of the wire. Parameters used in the simulation are: contact span $L' = 50$ mm, tension $T = 20$ N, slurry viscosity $\mu = 2500$ cP, wire bow angle $\alpha = 1.0°$, $NU = NP = 60$, and $NF = 100$. In the figure, the solid line represents the maximum vibration amplitudes at $V = 10$ m/s. The dashed line represents the maximum amplitudes at $V = 15$ m/s. The dotted line represents the maximum amplitudes at $V = 20$ m/s.

3. From Table 2, the effective damping of the first mode increases at higher speed of the wire. On the contrary, the effective damping associated with the second mode decreases at higher speed of the wire. Therefore, these different changes of the effective dampings affect the overall system response in different ways. Furthermore, the wire speeds used in the wiresaw process is within very limited range, and well below the critical speed. Hence, it has a negligible effect on the dynamics of the wire (see Section 2.1). In general, the wire speed does not affect the vibration characteristics of the wire/slurry system in the wiresawing process. On the other hand, wire tension remains a more dominant process parameter in the vibration of the wire/slurry system (also see Fig. 16 and Table 3).

Although lower wire speed is desirable in reducing the vibration of the wire, reducing the wire speed may not be practical due to the fact that the proper floating machining environment may break down if the wire speed is too low. In addition, the speed effect on vibration is not significant at low speed. In Section 5, we will address the vibration control issue by changing the tension of the wire.

Since the bow angles are small in the wiresawing processes, the wire tension is normally kept high (20–35 N) to generate a reasonably high nominal cutting force. Modal analysis has been

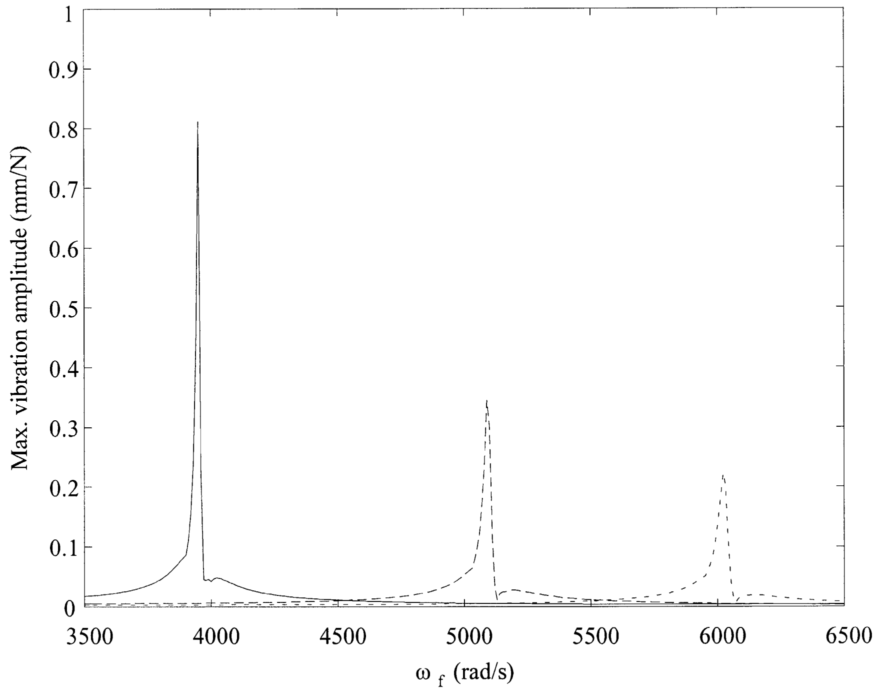

Fig. 16. Maximum wire vibration amplitude vs. excitation frequency at $T = 15$, 25, and 35 m/s. The wire vibration is more damped under higher tension. The damped frequencies increases significantly under higher wire tension. Parameters used in the simulation are: contact span $L' = 50$ mm, speed $V = 15$ m/s, slurry viscosity $\mu = 5000$ cP, wire bow angle $\alpha = 1.0°$, $NU = NP = 60$, and $NF = 100$. In the figure, the solid line represents the maximum vibration amplitudes under $T = 15$ N. The dashed line represents the maximum amplitudes under $T = 25$ N. The dotted line represents the maximum amplitudes under $T = 35$ N.

Table 3
First two underdamped modes under wire tension $T = 15$, 25, and 35 N

Wire tension T (N)	15	25	35
1st underdamped mode	$-45.0 \pm 3950i$	$-52.8 \pm 5094i$	$-59.4 \pm 6023i$
2nd underdamped mode	$-8.49 \pm 3953i$	$-16.0 \pm 5098i$	$-22.2 \pm 6030i$

conducted at three tension levels of 15, 25 and 35 N in order to study the effects of the wire tension on the vibration characteristics of the wire/slurry system. The first two vibration modes of the system are shown in Table 3. The maximum vibration amplitude of the wire is plotted against the excitation frequency in Fig. 16.

Some highlights of Fig. 16 and Table 3 include:

1. The real parts of the system eigenvalues associated with the first two modes decrease monotonically and rapidly when the wire tension is increased, which indicates higher effective damping. Therefore, the vibration of the wire is more damped under higher tension of the wire.

2. The damped frequencies of the wire/slurry system increases significantly under higher wire tension.

From the above simulation results, the vibration of the wire can be significantly reduced by increasing the tension of the wire, as it also was observed in Ref. [7]. This phenomenon is mainly caused by the increased transverse stiffness of the wire with higher tension.

4.1.3. Bow angle of wire and slurry viscosity

During wiresaw slicing, the nominal cutting force is generated through a proper bow angle of wire. This bow angle directly affects the quality of wiresaw slicing in many ways. For example, large bow angle of wire can result in the breakdown of the normal floating machining environment, and degenerate the slicing quality [16]. Modal analysis has been carried out at 4 levels of the bow angle, $\alpha = 0.5°$, $1.0°$, $1.5°$ and $2.0°$. Table 4 shows the first two vibration modes at these wire bow angles.

From Table 4, the real parts of the system eigenvalues decrease monotonically when the bow angle increases, which indicates higher effective damping. This implies that (1) the bow angle of wire also has significant effect on the vibration of the wire; and (2) the vibration amplitude of the wire decreases when the bow angle is increased. Therefore, larger bow angles are desirable in improving slicing quality to avoid excessive vibration of the wire. However, a too large bow angle of wire tends to cause the breakdown of proper hydrodynamic machining environment, especially at shorter contact spans [6,16,17].

The dynamic viscosity is an important mechanical property which characterizes the slurry in the wiresaw processes. This viscosity value is determined by different mixing ratios of the carrier fluid and abrasive grits. The viscosity of the wiresaw slurry ranges from tens to thousands centi poises (cP) [2,20]. To study the effects of slurry viscosity on the vibration characteristics of the wire/slurry system, modal analysis has been conducted using the viscosity values of $\mu = 2500$, 5000 and

Table 4
First two underdamped vibration modes at different bow angles of the wire

Bow angle α (deg)	0.5	1.0	1.5	2.0
1st underdamped mode	$-47.7 \pm 4665i$	$-50.6 \pm 4657i$	$-51.1 \pm 4651i$	$-52.0 \pm 4641i$
2nd underdamped mode	$-13.7 \pm 4666i$	$-14.4 \pm 4660i$	$-15.1 \pm 4657i$	$-16.4 \pm 4651i$

The parameters used in the analyses are: $T = 20\,N$, $V = 15\,m/s$, $\mu = 4500\,cP$, $L' = 60\,mm$, $NU = NP = 60$, and $NF = 100$.

Table 5
First two underdamped modes at different slurry viscosity $\mu = 2500$, 5000, and 7500 cP

Slurry viscosity μ (cP)	2500	5000	7500
1st underdamped mode	$-49.4 \pm 4553i$	$-49.1 \pm 4558i$	$-49.0 \pm 4559i$
2nd underdamped mode	$-12.9 \pm 4560i$	$-12.4 \pm 4562i$	$-12.3 \pm 4562i$

The parameters used in the analyses are: $T = 20\,N$, $V = 15\,m/s$, $\alpha = 1°$, $L' = 50\,mm$, $NU = NP = 60$, and $NF = 100$.

7500 cP, while keeping other process parameters constant. Table 5 shows the first two vibration modes of the system with different slurry viscosity.

From Table 5, the eigenvalues of the system do not change significantly within this range of slurry viscosity. This indicates that the vibration responses of the wire/slurry system also would not change much at different viscosity values, because the damping effect of slurry flow would increase with higher slurry viscosity, provided that the equilibrium film thickness remains the same. With higher slurry viscosity, however, a thicker slurry film tends to be developed between the wire and the ingot recess [1,6,16,17]. These two effects compensate each other. Hence, the damping force exerted on the wire by the slurry flow does not change very much with different viscosity values of the slurry.

5. Discussions

From our previous study of the equilibrium elasto-hydrodynamic interaction between wire and slurry flow [4,6,16,17], nominal wiresaw slicing is governed by the *rolling-indenting* process, which is a machining process similar to hydrodynamic polishing [24,25]. In other words, the nominal cutting force exerted by the bowed wire is transferred to abrasive particles via the hydrodynamic pressure within a slurry film of high viscosity. The equilibrium thickness of the slurry film is governed by the balance between the load exerted by the bowed and taut wire as well as the hydrodynamic pressure. The relation between the cutting load exerted by the wire and the hydrodynamic effort can be approximated by the geometric relationship given by Eq. (22).

In the industrial wiresaw process for wafer slicing, the surface quality of a round wafer is more sensitive to process parameter settings near the beginning and end of slicing, as discussed in Section 4.1.1. The following two observations are offered to explain this phenomenon:

1. From our FE analysis of the tribology of slurry flow, we found that at shorter contact spans, the thickness of the thin hydrodynamic slurry film is comparable to the average size of abrasive particle sizes [6,16,17]. Therefore, multiple direct or semi-direct contacts of the wire on abrasive grits upon the ingot surface can take place along the contact span for a sustained period of time, as suggested by the morphology shown in Fig. 11(b). The amplitude of vibration is expected to be high, too. As a result, nearly 100% of the nominal cutting load is transferred to the ingot surface by the multiple direct and/or semi-direct contacts, producing poor surface finish. On the other hand, when the slurry film becomes thicker as the contact span increases, a stable floating machining condition can be established with constant material removal rate. Under ideal floating machining condition, no cutting load is transferred to the ingot surface by direct contact of the wire on abrasive grits. Hence, the rolling-indenting machining dominates and results in a more homogeneous surface.
2. From the simulation results presented in Section 4.1.1, the wire has larger vibration amplitude at shorter contact spans, assuming the external excitation is constant in amplitude and frequency. Due to larger amplitude of vibration, the fluctuation of slurry film thickness and hydrodynamic pressure are also higher at shorter contact spans. Under floating machining conditions in the wiresaw process, this would lead to more variations in the material removal rate and surface roughness.

The preceding analysis suggests that extra care should be taken to control important process parameters adaptively during wiresawing in order to avoid excessive vibration of the wire and poor surface finish at shorter contact spans. In industry, such control is implemented in a piecewise continuous profile of feed rate based on experience and empirical results. However, we presented an analytical approach with numerical simulation to study various effects due to changes in process parameters. Such methodology can be employed to improve the performance of wafer slicing using a wiresaw.

From the parametric studies presented in Section 4.1, the tension and bow angle of the wire are identified as important practical parameters which can be controlled to reduce the vibration amplitude of the wire. Under floating machining condition of the wiresaw process, the vibration amplitude of the wire would be reduced by increasing wire tension and/or bow angle. From our previous studies [6,16], the bow angle of the wire is the key parameter in affecting the floating machining condition: proper floating machining condition may break down when the bow angle is too large, especially at shorter contact spans. Therefore, wire tension is the major parameter which should be controlled to avoid excessive wire vibration, provided a proper floating machining environment is established under a suitable wire bow angle. We divide the corresponding process variables into three ranges based on the length of contact span: short, medium, and large. For a 300 mm ingot shown in Fig. 17, for example, the three ranges are established: (1) short: $|y| > 141.4\,\text{mm}$, (2) medium: $111.8\,\text{mm} < |y| \leqslant 141.4\,\text{mm}$, and (3) $|y| \leqslant 111.8\,\text{mm}$. The following control strategy is suggested for the wiresaw process:

1. When the contact span is *short* ($\theta_1 < |\theta| \leqslant 90^\circ$): the bow angle should be small (1–3°) and the wire tension should be high ($30 < T < 35\,\text{N}$).

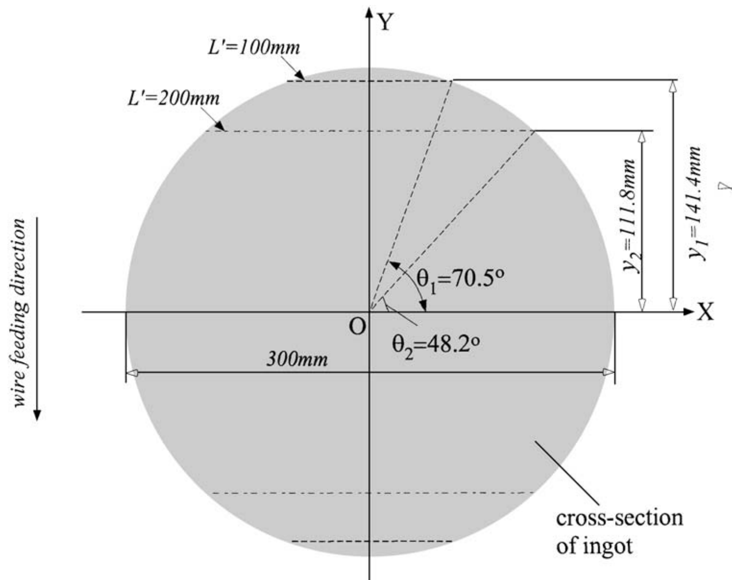

Fig. 17. Three ranges of contact span on the cross-section of a 300 mm ingot. θ is the angle from the $+X$-axis to the right end of a contact span. y is the distance between a contact span and the X-axis.

2. When the contact span is *medium* ($\theta_2 < |\theta| \leqslant \theta_1$): the wire bow angle can be medium (2–4°), and the tension of the wire can be either high or medium ($25 < T < 35$ N).
3. When the contact span is *large* ($0^\circ \leqslant |\theta| \leqslant \theta_2$): the bow angle and the tension of the wire can be any values provided they are within their typical ranges, and consistent with the requirements of slicing.

In the following, we summarize important results presented in this paper:

1. The vibration amplitude of wire is larger at shorter contact spans under normal floating machining condition, causing undesirable surface roughness. This is confirmed by the statistical measurement on surface roughness of wiresaw-sliced sample silicon wafers.
2. The effective damping of any vibration mode increases with the expansion of contact span between wire and ingot. In addition, larger wire tension also causes the effective damping to be larger.
3. The tension of the wire is identified as the important process parameter that can be controlled adaptively to prevent excessive vibration at short contact spans, which often results in poor surface finish. In general, high tension is desirable in reducing the vibration amplitude of the wire. Adaptive control strategies for consistent slicing of round wafers using wiresaws are proposed based on our analytical modeling.
4. Comparing with the tension of the wire, the wire speed is of minor importance in affecting the tool vibration characteristics in the wiresawing process. This is mainly because practical wire speeds are very low ($V = 10 \sim 15\,\mathrm{m/s}$) and well below the critical speed ($V \ll V_{\mathrm{cr}}$).
5. For the linearized wire–slurry system, the vibration of wire is asymptotically stable about its equilibrium position with typical wiresawing parameters and configuration. This conclusion can be extended to the original nonlinear wire/slurry system because the linearized system possesses *significant behavior*. Therefore, stability is guaranteed for the wire vibration in the normal slurry wiresaw processes.

6. Conclusion

In this paper, we study the vibration characteristics of the wire under hydrodynamic effects in the slurry wiresaw process. By modeling the interaction between the dynamics of the wire and hydrodynamic characteristics of slurry flow, the distributed non-conservative system is obtained through linearization about the equilibrium. To analyze the vibration response of the system, Galerkin-based discretization and subsequent modal analysis are employed. The Galerkin-discretized model is verified by direct time integration using a finite-element semi-discretization scheme. Applying the modal analysis to the Galerkin-discretized model, we studied the vibration responses of the wire, surface roughness of the sliced wafers as a function of contact spans, and the effects of various process parameters on the vibration of the wire.

Based on the modeling and analysis, we find that the effective damping due to the interaction between wire vibration and slurry hydrodynamics increases with the increase of contact span and wire tension, but decreases with the speed of the wire. It is also observed that the first two modes

of vibration in the wiresaw processes have frequencies that are close to each other, which is consistent with existing literature. Furthermore, the stability of the wire/slurry system in the wiresaw process is guaranteed because the linearized system possesses significant behavior. Based on the analysis, a practical strategy to adaptively control the process parameters to minimize poor surface finish was proposed.

Acknowledgements

The research has been supported by NSF Grant No. DMI-0085021.

References

[1] I. Kao, M. Bhagavat, V. Prasad, Integrated modeling of wiresaw in wafer slicing, in: *NSF Design and Manufacturing Grantees Conference*, Monterey, Mexico, January 5–8, 1998, pp. 425–426.

[2] I. Kao, V. Prasad, F.P. Chiang, M. Bhagavat, S. Wei, M. Chandra, M. Costantini, P. Leyvraz, J. Talbott, K. Gupta, Modeling and experiments on wiresaw for large silicon wafer manufacturing, in: *The Eighth International Symposium on Silicon Material Science and Technology*, San Diego, May 1998.

[3] I. Kao, S. Wei, F.-P. Chiang, Vibration of wiresaw manufacturing processes and wafer surface measurement, in: *NSF Design and Manufacturing Grantees Conference*, Monterey, Mexico, January 5–8, 1998, pp. 427–428.

[4] J. Li, I. Kao, V. Prasad, Modeling stresses of contacts in wiresaw slicing of polycrystalline and crystalline ingots: application to silicon wafer production, *Journal of Electronics Packaging* 120 (2) (1998) 123–128.

[5] R.K. Sahoo, V. Prasad, I. Kao, J. Talbott, K. Gupta, An integrated approach for analysis and design of wafer slicing by a wire saw, *Journal of Electronics Packaging* 120 (1998) 16–21.

[6] M. Bhagavat, V. Prasad, I. Kao, Elasto-hydrodynamic interaction in the free abrasive wafer slicing using a wiresaw: modeling and finite element analysis, *Journal of Tribology* 122 (2) (2000) 394–404.

[7] S. Wei, I. Kao, Vibration analysis of wire in free abrasive machining of the modern wiresaw manufacturing process, *Journal of Vibration and Sound* 231 (5) (2000) 1383–1395.

[8] F.Y. Huang, C.D. Mote, On the translating damping caused by a thin viscous fluid layer between a translating string and a translating rigid surface, *Journal of Sound and Vibration* 181 (2) (1995) 251–260.

[9] J.A. Wickert, Free linear vibration of self-pressurized foil bearings, *Journal of Vibration and Acoustics* 115 (1993) 145–151.

[10] J.A. Wickert, C.D. Mote, Current research on the vibration and stability of axially moving materials, *Shock Vibration Digest* 20 (1988) 3–13.

[11] J.A. Wicker, C.D. Mote, Classical vibration analysis of axially moving continua, *Journal of Applied Mechanics* 57 (1990) 738–744.

[12] J.A. Wickert, C.D. Mote, Response and discretization methods for axially moving materials, *Applied Mechanics Review* 44 (1991) S279–S284.

[13] F. Pellicano, F. Vestroni, Nonlinear dynamics and bifurcations of an axially moving beam, *Journal of Vibration and Acoustics* 122 (2000) 21–30.

[14] F. Pellicano, F. Vestroni, Complex dynamics of high-speed axially moving systems, *Journal of Sound and Vibration* 258 (2002) 31–44.

[15] E. Pesheck, C. Pierre, A new Galerkin-based approach for accurate non-linear normal modes through invariant manifolds, *Journal of Sound and Vibration* 249 (2002).

[16] L. Zhu, I. Kao, Equilibrium elastohydrodynamic interaction analysis in wafer slicing process using wiresaw, in: *Proceedings of IMECE'01*, No. EEP-24715, New York, November 11–17, 2001.

[17] L. Zhu, M. Bhagavat, I. Kao, Analysis of the interaction between thin-film fluid hydrodynamics and wire vibration in wafer manufacturing using wiresaw, in: *The Proceedings of IMECE'00: EEP-Vol 28, Packaging of Electronic and Photonic Devices*, Orlando, FL, November 2000, ASME Press, 2000, pp. 233–241.
[18] D.B. Marghitu, A. Guran, The dynamics of a flexible beam with a lubricated prismatic kinematic pair, *Journal of Vibration and Acoustics* 120 (4) (1998) 880–885.
[19] B. Bhushan, *Principles and Applications of Tribology*, Wiley, New York, 1999.
[20] HCT Corp, Annual report for wiresaw project, Technical report, GT Equipment Technologies, Inc., March 1997.
[21] A.V. Lakshmikumaran, J.A. Wickert, Equilibrium analysis of finite width tension dominated foil bearings, *Journal of Tribology* 121 (1999) 108–113.
[22] L. Meirovitch, *Principles and Techniques Vibrations*, first ed., Prentice-Hall, Englewood Cliffs, NJ, 1997.
[23] J.H. Ginsberg, *Mechanical and Structural Vibrations—Theory and Applications*, Wiley, New York, 2001.
[24] Y. Su, C. Hong, Y. Hwang, W. Guo, Effect of surface irregularities on machining rate of hydrodynamic polishing process, *Wear* 199 (1996) 89–94.
[25] Y. Su, S. Wang, J. Hsiau, On machining rate of hydrodynamic polishing process, *Wear* 188 (1995) 77–87.